N89-20957

INSTRUMENTATION ADVANCES FOR TRANSONIC TESTING

Percy J. Bobbitt
NASA Langley Research Center
Hampton, Virginia

SUMMARY

New and improved instrumentation, like new and improved wind tunnels, provide capabilities which stimulate innovative research and discovery. During the past few years there have been a number of instrumentation developments which have "aided and abetted" the acquisition of more accurate aerodynamic data and have led to new physical insights as well. The paper reviews some of these advances, particularly in the area of thin-film gages, hot-wire anemometry, and laser instrumentation. A description is given of the instruments and/or techniques and some sample results are shown. Finally, a few ideas for future research are described.

INTRODUCTION

There is an oft quoted statement by Ronald Smelt[1] in his Guggenheim Memorial Lecture of 1978 which reads in part "...in every aeronautical center, it is noteworthy that once the resource was available, there grew up around the facilities a group of people who knew how to use them, and use them wisely..." This observation loses very little of its accuracy if one substitutes the word "instruments" for "facilities". It may well be that he intended "facilities" to include instrumentation, for certainly they go hand in hand. Reference 2 includes both facilities and instrumentation in its list of research "drivers", which were defined as technologies or factors that stimulate research. The impact of new and improved instrumentation can be seen in nearly everything we do of an experimental nature. One can hardly attend an aerodynamics conference these days where instrumentation "breakthroughs" and innovative applications are not being displayed or discussed in some form. Therefore, it is appropriate in a conference which purports to make a statement about the state of the art of experimental transonic aerodynamics, that recent progress in instrumentation be the topic of at least one paper.

Over the past decade there has been a steady growth in the amount of diagnostic experimentation. This is being driven by the availability of new or improved instrumentation, data acquisition computers, and wind tunnel facilities as well as the ever increasing need/desire to validate fluid-dynamics computer codes. So in addition to the general benefits derived from improved or new instrumentation, code validation research will be a major benefactor.

Of particular interest in the present paper are improvements that have been made in several types of thin film gages, hot-wire anemometers, laser instrumentation, and a moving-band skin-friction gage. It will be shown that in many cases more accurate measurements can be made than just a few years ago

and, in others, measurements (or understanding) not previously possible can be acquired. The instruments will be discussed in the order just mentioned; some thoughts about future work will also be offered. Most of the research presented has been carried out or sponsored by the Langley Research Center (LaRC) Transonic Aerodynamics Division, and some was in collaboration with other LaRC organizations.

NOMENCLATURE

A	amplitude of boundary-layer disturbance
A_o	amplitude of boundary-layer disturbance at neutral stability
C_f	skin friction coefficient
C_L	lift coefficient
C_p	pressure coefficient
c	airfoil chord
E	mean voltage across hot film
e	fluctuating voltage
f	frequency
M	Mach number
m	mass flow
n	logarithmic exponent of T-S wave growth rates, $n = \ln (A/A_o)$
p	pressure
R	Reynolds number per foot, 1/ft
R_c	Reynolds number based on chord
R_θ	Reynolds number based on momentum thickness
SiO_2	Silicon Dioxide
S_{T_t}	$\left(\frac{\partial \log E}{\partial \log T_t}\right)_{u,\ \rho,\ T_w}$ or $\left(\frac{\partial \log E}{\partial \log T_t}\right)_{m,\ T_w}$
S_u	$\left(\frac{\partial \log E}{\partial \log u}\right)_{\rho,\ T_t,\ T_w}$

S_ρ	$\left(\frac{\partial \log E}{\partial \log \rho}\right)_{u,\ T_t,\ T_w}$
T	mean temperature
u	velocity in flow direction
v	velocity in vertical direction
w	velocity in horizontal direction
x	chordwise distance from leading edge of airfoil
α	angle of attack, degrees
δ_f	trailing-edge flap deflection
γ	ratio of specific heats
ρ	density
°R	degrees Rankine

Abbreviations:

Å	angstrom (10^{-10} meters)
COSAL	name of compressible boundary-layer stability code
Hz	Hertz, cycles/sec
IRD	Langley Research Center, Instrument Research Division
L	laminar
LDV	Laser doppler velocimeter
LTPT	Low-Turbulence Pressure Tunnel
mv	milli-volt
NAE	Canadian Natural Aeronautical Establishment
NLF	natural laminar flow
NTF	National Transonic Facility
SALLY	name of incompressible boundary-layer stability code
T	turbulent
TCT	Transonic Cryogenic Tunnel
T-S	Tollmien-Schlichting

Superscripts:

$\sim$	root-mean square value
-	mean value
'	instantaneous value

Subscripts:

aw	adiabatic wall
max	maximum value
T	end of transition
t	total condition also start of transition
tr	value at transition
w	wall
∞	free-stream conditions

THIN-FILM SENSORS

The use of thin-film (or hot-film) sensors spans a number of decades with application to both heat transfer and transition. In recent years the increase in the amount of laminar-flow experimentation has resulted in a corresponding increase in the use of thin-film sensors. Tests of laminar-flow airfoils and wings are greatly enhanced if they include a determination of where transition takes place. Of nearly equal importance is the identification of the most amplified frequency since it is this quantity that determines transition as predicted by classical stability theory. In the subsequent sections a variety of thin-film gages will be discussed with some sample data to indicate the type of information that one can extract using these gages.

Patch Thin-Film Gages

Transition detection has been accomplished using stick-on or patch gages individually or in arrays. The latter permits the mapping of transition zones or the monitoring of the movement of transition as flow conditions change. A row of patch gages on a laminar-flow airfoil model in the Low-Turbulence Pressure Tunnel (LTPT) and on a laminar-flow wing (Cessna 210 with laminar glove) are shown in figures 1(a) and 2, respectively. Figure 1(b) shows an enlarged photograph of the patch gages on the airfoil model in the LTPT and the trailing flexible leads connected to terminal blocks. Each thin-film patch gage will cause transition; consequently, downstream gages must be displaced laterally to make an uncontaminated measurement.

Normally, one looks at the amplitude and character of the output signals to make a determination if the flow is laminar, transitional, or turbulent. This was done in both the wind tunnel and flight experiments, and transition was easily detected. Transition-location results from these investigations are plotted in figure 3 including several points determined from sublimating chemicals in flight. When these data are compared with each other and to calculated results from incompressible stability theory, it is evident that they all agree quite well.

The LTPT test mentioned above had an additional significance since it was during the course of this investigation that J. P. Stack[3] showed for the first time that these gages were sensitive enough to enable the detection of the most amplified frequency. Figure 4 gives the spectrum from one of the patch gages of the LTPT tests and clearly shows that a Tollmein-Schlichting wave of 1.4 KHz was the most amplified frequency. Stability calculations carried out for the same conditions as the test (right side of figure 4) also indicated that the most amplified frequency was in the vicinity of 1500 Hz and added credibility to the discovery.

Patch gages have also been employed in flight tests[4] and produced results similar to those obtained in the wind tunnel except they are for a higher Mach number (M = 0.79). The experiments were carried out on the top side of the wing of a Lear 28/29 as pictured in figure 5. Several gages were located at a number of chordwise locations but most of the data were obtained at the 30 and 40 percent chord locations. Power spectra obtained at these two locations are shown in figure 6 and, as in the wind tunnel tests (figure 4), the most amplified frequencies are easily seen. These frequencies, however, are in the range of 4 to 5.5 thousand, which are much higher than those encountered at low speed. Another noteworthy feature of the data of figure 6 is the amplification in the range of 8.35 to 11.10k Hz.

Stability calculations were carried out with both incompressible and compressible codes using the measured distribution and the results displayed in reference 4. Figure 7, taken from this reference, shows the experimental pressure distribution and the wave amplification ratio (n factor) for a range of frequencies up to 7000 Hz, calculated using the SALLY incompressible code. The most amplified frequency is 5600 Hz which is in good agreement with the thin-film data; the corresponding n factor is approximately 8.3. Compressible calculations using the COSAL code indicate an n factor of 3.9 at transition which is much lower than most would expect.

Plug Thin-Film Gages

Plug type gages can be used in the same way as patch gages[5] but have the added advantage that they are flush with the surface and, unlike the patch gages, do not cause transition. Consequently, one gage can be placed directly downstream of another. Their disadvantage is that they are more difficult to install. The laminar-flow control (LFC) airfoil experiment in the 8' TPT utilizes plug gages[6,7] to determine the regions where the flow is laminar or turbulent. Figure 8 shows an enlarged picture of a plug-gage installation where the plug gages are made of quartz with a diameter of 0.06 in. A map of the surface of the LFC airfoil with the letters L and T at the various gage locations to indicate the state of the flow for a particular test is given on

the left side of figure 9. On the right of figure 9 are typical time traces of the voltage output from gages as one moves from the laminar region (bottom of figure) through the transitional zone and finally (top of figure) to the turbulent flow near the trailing edge. These gage outputs are monitored in real time as an aid in adjusting the suction distribution on the airfoil. In addition, the signals are electronically analyzed to determine the state of the boundary layer at each gage for recording.

Surface Deposited Thin-Film-Gage Arrays

For wing or airfoil models with chords of just a few inches, neither patch or plug gages are appropriate. However, there are several gage, or sensor, array concepts that have been invented which are quite capable of "filling the bill." One of these is the McDonnell-Douglas developed vapor deposited hot-film gages and gold leads all on an epoxy dielectric substrate (see figure 10). A photograph of an airfoil model equipped with these films installed in the Langley 0.3-Meter TCT is given in figure 11(a) in which the gold leads are clearly visible; the sensor itself can be seen in the enlarged picture in figure 11(b). Of course, some means of carrying the electrical signals from the gold leads to the anemometer cables must be provided. Figure 12 shows a picture of the end of the airfoil model where the contact points are labeled and the anemometer leads can be easily seen.

Typical results from the 0.3-M TCT are presented in figure 13 taken from reference 8. Shown in figure 13(a) is a typical pressure distribution for a Mach number of 0.6, R_c of 7.5 x 10^6, and angle of attack of -4°. Figure 13(b) gives, for the same free-stream conditions, the normalized RMS voltages for eight sensors along the chord of the supercritical airfoil at adiabatic wall conditions. The fluctuating voltages from each of these gages is also given. The gage nearest the leading edge indicates a very low amplitude oscillation indicative of laminar flow while the second indicates short periods of laminar flow followed by turbulent bursts (large voltage spikes). At an x/c of 0.2, the location of the forth gage, the flow has become fully turbulent. Data for several Mach numbers and T_w/T_t ratios are given in reference 8 and clearly demonstrate the viability of the vapor deposited sensors.

Despite the success of the 0.3-M TCT tests, a large number of gages were lost and it was clear that some improvements to the gage system were desirable. After considerable effort and numerous trials, a new metalization process was formulated[9]. It has a 0.0003 inch dielectric substrate of parylene C, which also serves as a strain isolation pad, covered by an even thinner layer of silicon dioxide SiO_2 (see figure 14). The hot-film sensor and leads are deposited on the SiO_2 and are composed of nickel and aluminum, respectively. Aluminum is used instead of gold because it adhears to the SiO_2 much better than gold.

Proof of concept tests were carried out in the NTF with a sidewall mounted model as shown in figure 15 and in a small calibration tunnel with the model shown in figure 16. The NTF model used a 20% thick symmetric airfoil with an 8 inch span mounted on the tunnel side wall. Tests of this model showed that the new hot film and substrate materials worked well together at both ambient and cryogenic temperatures (down to -247° F).

The model used in the low speed calibration tunnel, shown in figure 17, had a NACA 0012 airfoil section, a 12-inch chord, and a 12-inch span. A slot was cut in the upper surface for a 3-in. by 10-in. aluminum insert on which 30 hot-film gages were deposited (figure 18). Normalized RMS voltages from a number of sensors along the chord of this model are plotted in figure 19. Free-stream conditions are M_∞ = 0.122 and an angle of attack of zero degrees (R_c = 0.86 x 10^6). Also shown in figure 19 are time traces of the voltage output to indicate the signal differences that go with laminar, transitional, and turbulent flow. Spectral analysis of three of these signals near the onset of transition yield the curves in figure 20. Of particular note here is the peak near 2.5 KHz which was the frequency predicted to be the most amplified.

In summary, a technique has been developed to deposit a dielectric, hot-film gages and leads on a model surface, which will function at cryogenic temperatures and has the potential for providing much needed transition data at high Reynolds numbers at transonic speeds. However, tests on wings on complete aircraft models in a cryogenic wind tunnel are still required to firmly establish this form of thin film technology.

Thin-Film-Gage Arrays on Polyimide Substrate

Another thin-film array concept which is being developed consists of a number of individual nickel films electron-beam evaporated on a thin (0.05 mm) polyimide substrate (figure 21).[10] Each sensor consists of a Nickel film 0.9-mm long and 0.15-mm wide with 50 micron copper-coated nickel leads routed to the attachment point of the anemometer leads. The films may be positioned very close together in a single row or a number of rows, and they can be aligned either with the chord or on a diagonal. One of the first arrays using the very small spacing is shown in the photograph of figure 22 where 30 sensors are mounted at 0.1-inch intervals. It was bonded to a low-speed natural laminar-flow (NLF) airfoil with a chord of 15 cm and with the sensors positioned in the streamwise direction on the top surface. The first sensor is located at 0.45 c and the last at 0.95 c.

The leads of the sensors shown in figure 22 run to the trailing edge where they are taken out to the anemometer. Clearly, this arrangement was not meant to provide definitive force and moment data but to prove the sensor-array concept and investigate the characteristics of the gage outputs. The 30 gages in the array were scanned in groups of 8 since only 8 anemomenters were available. A multichannel switch was used to connect the desired sensor group to the constant temperature anemometers which simultaneously heated the film to a nominal 50°C (122°F) above recovery temperature. This required only a small amount of heat and the heated thin films cause little disturbance to the shear layer or to each other. This was established by heating each sensor individually and in groups, with the downstream sensor maintained at a cold temperature. The sensor signals were amplified by an A-C coupled amplifier and recorded on an analog tape recorder. Signals from the amplifier were also provided to an array of oscilloscopes to provide on-line time-history traces.

The NLF airfoil used in the test is designated LRN(1)-1010 and was chosen because of its known laminar separation characteristics at low Reynolds number. Pressure distribution on this airfoil obtained in a low-speed tunnel at a Mach

number of 0.06 and a Reynolds number of 200,000 are plotted in figure 23. A separation bubble exists at all angles of attack plotted in the vicinity of 0.70c.

Typical time histories from the thin-film gages at different locations along the chord of the airfoil are shown in figure 24 beginning with the "laminar-flow" signal at x/c = 0.467. Time traces are given for a location further downstream, just past separation (x/c = 0.667), at the beginning of transition (x/c = 0.717), at peak separation (x/c = 0.750), and finally at reattachment (x/c = 0.883). An interesting discovery reported in reference 10 was that if only the low frequency components (< 20 H_z) of the signals are retained, one can see a clear phase reversal of the signals from gages on either side of separation. Figure 25 shows this effect where the signals ahead of and downstream of x/c = 0.65, the separation point, are out of phase. The same type of signal reversal occurs at reattachment.

An analysis of the spectra of a signal trace from a gage near the onset of transition has been carried out to demonstrate that the present sensors also have the sensitivity to detect the most amplified T-S frequencies which lead to transition. Figure 26 shows the auto correlation of the thin-film signals of the gage at x/c = 0.6 and the results from a boundary-layer stability calculation using the SALLY code. Clearly the most amplified frequencies from the experiment are in the range of 1000 to 2200 Hz; the theoretical frequencies are in the same range.

Tests of an improved gage array on the polyimide substrate were carried out in the Langley Low-Turbulence Pressure Tunnel (LTPT).[11] The multielement sensor leads in this test ran spanwise (see figure 27) so that the anemometer leads were connected at the tunnel wall and, consequently, the flow was not distorted at the trailing edge as was the case for the prototype configuration. Another difference of these tests was the airfoil model, which had an Eppler 387 section and a 6-inch chord. The results obtained in the LTPT test were similar to those described previously; separation and reattachment were easily detected. Figure 28 showing filtered and unfiltered signals in the vicinity of reattachment shows the low energy signal at reattachment, x/c = 0.687, and the signal reversal on either side. Phase correlations of the signals from the gages on either side of reattachment and separation confirm the reversals.

The tests of the polyimide based thin-film gages described preivously have all been low speed. High-subsonic speed tests have also been carried out in the 0.3-M TCT to look not only at separation and reattachment but to explore the possibility that new diagonostic information related to the supersonic zone and shock interaction could be obtained from the thin-film signals. Films were bonded on both the top and bottom surface of the airfoil depicted in figure 29(a) but, for a number of reasons, only a few of the gages on the upper surface were operative throughout the tests. Gages on the lower suface yielded some interesting results; a sample is described below.

A test was run with the airfoil of figure 29(a) at an angle of attack of -1.0° and a Mach number of 0.7 (R_c = 6 x 10^6). The resulting lower surface pressure distribution is plotted in figure 29(b) and shows a shock in the vicinity of x/c = 0.33; resolution does not permit a precise determination. If one looks at the gage outputs in this region (see figure 30) and phase

correlations between successive gages (figure 31), it is clear that there is a small separation bubble beneath the foot of the shock. The separation point is somewhere between x/c of 0.326 and 0.343 (see phase reversal in figure 31(c)), and reattachment occurs between x/c = of 0.343 and 0.359 (see phase reversal in figure 31(d)). A close look at the time traces for a long period of time indicated that there is shock unsteadiness and bubble movement. Even though data reduction and analysis of the present test results have just begun, it is clear that more tests are needed at transonic speed including, if possible, some complimentary flow visualization activity.

The development of multielement dynamic shear stress sensors and the discovery of the phase reversal phenomenon at flow separation and reattachment have opened up new avenues for studying surface shear-flow characteristics in ways that were considered impossible until recently. It should now be possible to obtain detailed surface flow characteristics in such hard-to-reach locations as turbomachinery blades and junctures as well as on very thin surfaces. In view of the ability to make simultaneous measurements, the new technique can be used with equal ease for steady as well as unsteady flow conditions and has enormous potential for both ground and flight test applications. Since the entire surface flow field can be mapped, with the right equipment, in "one fell swoop," the time required to conduct an experiment is remarkably small compared to all other existing techniques which are more cumbersome and time-consuming.

Another possible application of thin-film arrays is to determine the direction of the most amplified wave. This is an important quantity at transonic speeds where stability theory predicts that waves propagating at up to 50° or 60° from the stream direction are the most amplified. A gage array with perhaps 5 or 6 rows and twenty sensors on a row could yield the necessary solutions.

HOT-WIRE ANEMOMETRY

Through the 1950's and 60's progress in hot-wire anemometry was aided by advances in computers and electronic equipment, but improvement in the accuracy of results was hindered by assumptions in the data reduction methodlogy. It was the consensus that the problems due to these assumptions were confined to compressible subsonic and transonic flows where mean flow measurements indicated that the voltage measured across a heated wire oriented normal to the flow was a function of velocity, density, and total temperature.[12-17] Several papers were published in the mid seventies by Rose, McDaid, and Horstman[18,19] which reported on results which indicated that the mean voltage across a heated wire was only a function of mass flow and total temperature. Assuming this to be true, they formulated a two probe technique for temperature and mass fluctuations which made the determination of the velocity, mass flow, and density fluctuations tractable.

In 1980 Stainback[20] outlined a new technique utilizing a three wire probe (see figure 32), each with different overheats and a solution technique accounting for sensitivities to velocity, density, and total temperature. For a constant temperature hot-wire anemometer the equation for the instantaneous voltage ratioed to the mean is given by[20]

$$\frac{e'}{E} = S_u\left(\frac{u'}{u}\right) + S_\rho\left(\frac{\rho'}{\rho}\right) + S_{T_t}\left(\frac{T_t'}{T_t}\right)$$

where S_u, S_ρ, S_{T_t} are the sensitivity coefficients. Stainback's approach is to solve equation (1) for the instantaneous value of u, ρ, and T_t. Sensitivity coefficients are obtained from a mean flow calibration and curve fitting techniques; e and E are measured. Solution of the sensitivity-coefficient matrix is abetted by operating the three wires at different overheats provided the heat transfer characteristics of the wires are similar. Additional details of the method and error sources are given in references 20 and 21.

Some results of applying the "3-wire" technique to flow quality measurements in the Langley 0.3-Meter Transonic Cryogenic Tunnel are given in reference 20. It was shown that the sensitivity coefficients for density and velocity are not the same, as often assumed in the past, with that for density generally being higher than that for velocity. It was also demonstrated in reference 22 that mass flow fluctuations were very much less than the velocity fluctuations due to the fact that at high subsonic Mach numbers most of the disturbances are moving upstream from the diffuser. Because of this, u'/u and ρ'/ρ are anti-correlated and the mass flow fluctuations are reduced. Thus, the use of mass flow fluctuations as an indicator of tunnel disturbance levels was shown to be inappropriate.

In the past few months, a flow-quality survey of the Langley 8-foot Transonic Pressure Tunnel has been made utilizing 3-wire and single wire probes and associated data reduction techniques. Data were obtained in the test section using 3-wire probes and in the settling chamber using single wires. Probes were located in a number of locations in the test section but the location which was thought to give flow-quality data that was most representative of that seen by the "laminar" test region on the laminar flow control (LFC) airfoil was one that was ahead of the airfoil 2 1/2 feet off the side wall and 3 feet above the floor. Figure 33 shows this installation with the LFC airfoil downstream of the probe holder.

A 3-wire probe was calibrated on this rake by holding pressure and temperature constant and varying Mach number then changing pressure at the same temperature and repeating the Mach sweep. Temperature was then changed and the process repeated. Data for four pressure levels at a fixed temperature and three temperatures at a fixed density was obtained. Example plots for one of the wires for the variation of S_u, S_{T_t}, and S_ρ with $\log(\rho)$, $\log(u)$, and $\log(T_t)$ respectively are given in figure 34(a). These plots were obtained using a curve fit technique and can be inserted in equation (1) along with those for the other two wires and a 3- by 3-matrix solved for the instantaneous values of ρ, u, T_t, with the voltage from each of the three wires for input. Subsidiary equations allow for the determination of m and p as well.

There are a number of different approaches for using a single wire for the determination of $\tilde{u}/u$. Most require the assumption that the sensitivity of the wire to density and velocity be the same. In one approach, calibrations are done with mass flow and a single sensitivity curve that grossly approximates the points obtained by varying pressure (if one uses a pressure tunnel) and u. This type of approximation is labeled Method I on figure 34(b) and works best at very low Mach numbers where the data tends to collapse on a single line.

A second approach (Method II) uses the slope of the data in the vicinity of the Mach number and pressure of the test. Figure 34(b) shows this approximation for a pressure of 710 psf. This gives a representation of the log(E) dependence on log(ρu) that is quite good for Mach numbers below 0.6. If one takes the slope of the data at $M_\infty = 0.65$ where log(E) is a maximum, then the sensitivity will be zero and the Method will yield ridiculous values of u'. Results for the 3-wire technique and both Method I and II for single wires are discussed below.

Using the 3-wire sensitivity coefficients just described, the RMS values of $\tilde{u}/u$, $\tilde{\rho}/\rho$, $\tilde{T}_t/T_t$, $\tilde{m}/m$, and $\tilde{p}/p$ have been determined for Mach numbers for 0.4 to 0.82. Values of these quantities for a probe location discussed previously (see figure 33) are given in Table I. If one of the wires is treated as a single wire using single-wire data-reduction assumptions, the sensitivity coefficient of Method I and

$$\frac{\tilde{u}}{u} = \frac{\sqrt{\overline{(m'/m)^2} + \overline{(p'/p)^2}}}{[1 + (\gamma - 1) M_\infty^2]}$$

then the values for $\tilde{u}/u$ and $\tilde{m}/m$ labeled 1-wire are obtained. Finally, in the last column of Table I are values of $\tilde{p}/p$ obtained from a microphone in the probe.

Several things stand out in Table I. One is the large differences in the values of $\tilde{u}/u$ and $\tilde{m}/m$ between the 3-wire and single wire results. Another is large differences between the 3-wire $\tilde{p}/p$ and that of the microphone. It must be remembered in looking at these data that most of our thinking relative to what constitutes good flow quality is based on single wire and microphone data. If, in this case, we were to use single-wire thinking in interpreting the single wire data, we would conclude that we have "pretty good" flow quality. On the other hand, if we use single-wire thinking and the 3-wire data we would say we have poor flow quality. The fact is that a whole new set of standards has to be created to decide what is good and bad flow quality when using the 3-wire data.

Another look at single wire data is afforded by figure 35 where $\tilde{u}/u$ and $\tilde{m}/m$ from Method I and II are plotted as a function of free-stream Mach number along with $\tilde{p}/p$. The levels are what one would expect in a good flow quality tunnel and, at the highest Mach numbers where the test section is choked ($M > 0.75$), the levels from Method I are outstanding. The large effect of the "choke" on the levels is clear and, indeed, what most would expect.

Values of $\tilde{u}/u$ from Method II are quite a bit higher than those of Method I but are still an order of magnitude lower than those produced by the 3-wire techniques. A quite different picture emerges if we examine the 3-wire $\tilde{u}/u$ data plotted in figure 36. It is obvious that 3-wire levels are 3 to 4 times higher than those of the single wire and that the choke is less effective. The drop in magnitude of $\tilde{u}/u$ is about the same in each case but the 3-wire level is so high that the relative effect of the choke is much smaller.

Only a few flows have been examined using the 3-wire hot-wire probe. A much larger data base must be created to provide the understanding that will enable the formulation of new standards. One contribution to this understanding will come from an experiment in the Basic Aerodynamic Research Facility to be described later. In this experiment a 3-component LDV will be used along with a 3-wire probe to provide two independent measurements of $\overline{u/u}$.

LASER INSTRUMENTATION

Laser velocimeters have been in use for over 2 decades in fluid flow research starting with the work of Yeh and Cummin in 1964.[23] Most of the systems producing data since that time have been 2-component systems and used primarily for mean-flow velocity measurements. Some systems employed forward scatter, others back scatter and within these two-categories a number of different techniques/systems were developed. At Langley 2-component systems have been installed in the 14- by 22-Foot Subsonic Tunnel for helicopter and turboprop flow-field research, in the Vortex Facility for trailing vortex diagnostics and in the 16-Foot Transonic Tunnel for flow-field surveys.

In this section several types of 3-component LDV systems that have been used at LaRC for flow-field surveys will be discussed followed by a description of a laser interferometer being developed for transition measurements. Finally, a short section is included to show some recent results from the use of a laser vapor screen.

3-Component Single Axis LDV

The first use of a 3-D LDV used at this Center for 3-component mean and fluctuating flow-field data was in the LTPT for a juncture-flow investigation.[24,25,26] The system used was a single axis, five-beam optical configuration and is shown in the photograph in figure 37. Optical access was only through a side window in the tunnel test section and precluded the use of an off-axis system. The data obtained from the juncture-flow experiment was highly accurate on the u and v axis but less so on the w axis due to the small beam angle.[27]

A second application of the LDV system of figure 37 was in a study of Taylor-Görtler instabilities in a concave region of the airfoil pictured in figure 38.[28] The airfoil model was equipped with a suction panel in the concave region and patch transition gages just beyond the suction panel. A small sample of the laser results obtained are plotted in color-coded contours in figure 39. Shown in this figure are the mean (top of figure) and fluctuating (bottom of figure) components of the horizontal velocity measured adjacent to the surface in, and just beyond, the concave region. The periodic nature of the vortex spacing is very clear in the LDV measurements and further substantiated by the sublimating-chemical flow visualization pictured in figure 40. Wavelength data from both of these sources (flow visualization and laser) are plotted in figure 41 as a function of unit Reynolds number. Also shown for comparison is the theoretical prediction of Floyan.[29] The figure indicates that the theory agrees with both the laser and flow visualization measurements.

Orthogonal 3-Component LDV

The angle betweem the beams yielding the w, or lateral, velocity component should be made as large as the optical access will permit[28] with an orthogonal arrangement such as that pictured in the photograph of figure 42 yielding the best accuracy. This figure shows the LDV system which has been installed in the transonic Basic Aerodynamic Research Facility (BARF) during its laboratory checkout. Figure 43 shows the same system wrapped around the glass-walled test section of BARF. A better view of the test section is afforded by the photograph in figure 44(a) where the test section with a wall interference model mounted on a sting is shown. Both side walls and the top of the test section are glass; the cross section is 18-in. x 18-in and the length is 55-in. Figure 44(b) gives a sketch of the main components of the BARF including the contraction, test section, plenum, and high-speed diffuser.

The BARF was specifically modified to make 3-D LDV measurements with a system as accurate as technology permits in order to compare LDV measurements with those obtained by multiwire hot-wire anemometers at transonic speeds.[30] A variety of basic attached and separated flows will be "measured" and accuracy relation judgments made where possible. In this connection it is anticipated that high order viscous flow calculations will be an equal partner in many of the accuracy assessments.

The first measurements made in the BARF were of the "free-stream" flow quality in the test section. Some selected data for the RMS unsteady component of the longitudinal velocity are plotted in figure 45 and are preliminary in the truest sense of the word (they were otained just a few days ago). Transients in the tunnel circuit, uniformity of seeding, and the effects of the tunnel vibration and acoustic environments still need to be investigated. The scatter in the LDV data at Mach numbers of 0.4, 0.45, and 0.5 are much larger than one can attribute to instrument accuracy. Repeatability at Mach numbers of 0.1 and 0.2 was excellent; each of the plotted points represents several test points.

The reason for presenting this preliminary data is to make a comparison of the LDV data with that of the 3-wire and 1-wire anemometers. Clearly the LDV and 3-wire measurements of $\tilde{u}/u$ agree quite well in level. Both are at variance with the single wire results obtained using Method I. It should be noted that mean values of the longitudinal velocity obtained by the LDV are in excellent agreement with the values obtained from the pressure system used to determine Mach number in the test section. Further experimentation in this facility will, no doubt, lead to a better understanding of both the laser and 3-wire results.

Laser Interferometer for Transition Measurement

Responding to the need for measurements of boundary-layer transition during wind tunnel experiments, NASA Langley has developed under contract an optical interferometer to nonintrusively detect transition in compressible boundary layers. The device is a highly sensitive differential interferometer capable of detecting optical path-length differences of less than one-thousandth of the wavelength of the laser light.

The interferometer uses a 5-mW helium-neon laser for its light source (see figure 46). The beam is passed through a polarizing plate and then into a Pockels cell, which is aligned 45° from the direction of original polarization and effectively produces two orthogonally polarized beams. In addition, the Pockels cell provides a means of creating a phase difference between the two beams so that the instrument operates at its greatest sensitivity (see reference 31). The beam expander and lens provide a collimated beam to the beam splitter and Wollaston (1). Wollaston (1) acts as a prism that deflects one of the two orthogonally polarized beams by a predetermined angle. The two beams then pass through the boundary layer on the model (see figure 47) at different locations. Differences in density fluctuations in the boundary layer at the two model locations manifest themselves as optical path length differences.

Light reflecting back from the model surface returns through the lens and Wollaston (1) and is directed by the beam splitter to Wollaston (2) and the two photodetectors. The photodetectors generate the signal voltage, which is a function of optical path length differences between the two beams, and also provide information back to the Pockels cell for adjusting the relative phase between the two beams for optimal interferometer performance. On the basis of the thin-film data previously discussed and traversing pitot pressure probe studies by Dougherty in reference 32, the fluctuations in voltage signal are expected to be minimal for a laminar region, to reach a maximum in the transitional region, and fall again to a lower level in the fully turbulent region.

An important evaluation of the instrument occurred during June of 1986 when it was tested in the Boeing Model Transonic Wind Tunnel at a Mach number of 0.7. As seen in figure 48, the instrument was set up on an optical bench next to the tunnel and the beams entered the tunnel normal to the test section sidewall. A 6-inch NACA 66-006 airfoil was mounted between the bottom and top walls so that the beams struck the airfoil in a direction approximately normal to its surface. As seen in figure 49(a), the RMS output signal values vary as expected for natural transition along the airfoil. Its value is initially minimal near 3.5-inches from the leading edge, where laminar flow is expected to be present. However, as transition begins to take place in the boundary layer, the level of fluctuations increases until a maximum magnitude is reached near 5-inches, which is assumed to be the location of greatest unsteadiness in the transitional region. Further downstream at 5.75-inches, where the flow is becoming fully turbulent, the RMS level has dropped below its maximum value and appears to be approaching an intermediate level.

For comparison purposes, a separate flow visualization run was done with sublimating chemicals and the beginning of the scrubbed region was found to coincide, within experimental error, with the location of the maximum signal RMS of the interferometer (see figure 49(b)). Even though there may be no fundamental reason why these two positions should coincide, the instrument is recording peak activity in the same region that sublimating chemicals would suggest transition occurs.

Finally, this promising technique for unobstrusive measurement of boundary-layer transition will be further investigated at the Langley Research Center during 1988 as part of an assessment of boundary-layer transition measurement techniques to be conducted in the Unitary Plan Wind Tunnel at supersonic speeds. The results of the optical interferometer will be compared, during the same test, to techniques such as liquid crystals, infrared photography, and hot-film anemometers.

Laser Vapor Screen for Flow Visualization

Another application of laser technology to diagnostic measurements is the vapor screen. The vapor screen technique is a simple, yet effective, flow visualization tool used to study the off-body flows about aerodynamic shapes at subsonic, transonic, and supersonic speeds. In recent years, this technique has frequently been employed in wind tunnel experiments to improve the understanding of the vortices shed from the slender bodies of missiles and the fuselage forebodies and wings of fighter aircraft at high angles of attack. The technique features the injection of water into the tunnel circuit to create a uniform fog in the test section and a laser generated intense sheet of light that can be oriented in any selected plane relative to the test model. The light is scattered as the water particles pass through the sheet, which enables the off-body flow to be visualized.

Figures 50 and 51 show representative results from a NASA experiment that were obtained using a laser vapor screen technique in the David Taylor Research Center's (DTRC) 7- by 10-Foot Transonic Tunnel. The model is a general research fighter configuration having a 55° cropped delta wing and slender, sharp-edged forebody chines, or strakes. A beam of coherent light generated by an 18-watt argon-ion laser was directed to a set of optics located in a window in the right side of the test section. The beam passed through a line generator, or cylindrical lens, and the resultant sheet of light "sliced" through a model cross-plane located approximately 75 percent of the distance along the wing centerline chord measured from the apex. This position coincided with a spanwise row of upper surface static pressure orifices on the right wing. Figure 50 illustrates the cross flow as observed from a three-quarter right rear view, corresponding to an angle of attack of 30° and a free-stream Mach number of 0.95. The laser light sheet illuminates the vortex pair generated by the forebody chines. The dark areas within the donut-shaped structures define the location of the vortex centers, which are essentially devoid of water particles. The wing leading-edge vortices are also present, but are not well-illuminated due to the side-scatter orientation. Figure 51 shows the flow structure in the same cross-plane at an angle of attack of 20° and a free-stream Mach number of 1.10. The 35-mm still camera was positioned in a three-quarter left-rear view. The vortex pair from the forebody chines is again depicted. Due to forward scatter, the right wing leading-edge vortex is now clearly visible as a flat, elliptically-shaped region within which water particles are noticeably absent. The left wing vortex is not seen since it is located in the shadow created by the center fuselage.

Articulation of the laser-system platform or the optics has been used in some investigations to look at the entire flow field.

MOVING BELT SKIN FRICTION BALANCE CONCEPT

The principal of operation of the moving belt skin friction balance developed, under Langley grant, by the University of Tennessee Space Institute (UTSI) can be illustrated with the aid of figure 52. The balance is mounted such that the belt is flush with the surface to be investigated. The two drums that support the belt are, in turn, supported by flexures. When the belt experiences force due to the shear of a passing fluid, it rotates the drums against the restoring force of the flexures. The stiffness of the flexures is

selected to allow a maximum of 3° of rotation for the expected forces. Strain gages are attached to the flexures to produce a voltage proportional to, and linear with, the torque produced by the belt rotating the drums. Since the small gaps that are open to the flow do not change with this rotation, there is no need for a closed-loop nulling device to center the measuring element as there is in the floating element type balances. Further details are available in reference 33.

The moving belt gage has been used to make measurements in several wind tunnels to determine it capabilities. One such test was carried out in the 0.3-M TCT on the test section sidewall as part of an investigation designed to evaluate the performance of several skin friction measurement devices in a cryogenic, transonic environment. To insure a minimum of disturbance during these tests there was no model mounted in the tunnel. Special care was taken in mounting the gage to minimize boundary-layer disturbances; however, the data exhibits a rough wall trend, i.e., very little change in C_f with increasing Reynolds number. It is instructive to consider the distributed-wall roughness height which would be required to "fit" the observed data. Plotted in figure 53 are curves representing a range of values for roughness height; values in the range from 0.005 to 0.02 mm (0.0002 to 0.0008 inches) are typical of the data. The figure serves to demonstrate the severe effects of small roughness heights in a turbulent boundary layer, and that an equivalent roughness height of only 0.02mm is sufficient to match the data.

The approximate formula for rough flat plate flow used to generate the curves was

$$C_f = (2.87 + 1.58\log(x/\varepsilon))^{-2.5}$$

where ε is the roughness height and x is distance from the leading edge.[34] Reference 35 discusses the details of applying this formula to a test section wall boundary layer, by calculating an equivalent flat plate length. The curve labeled smooth in figure 53 was calculated from the relation

$$C_f = 0.027/(Re_x)^{1/7}$$

also from reference 34.

Current plans call for further testing of UTSI balances on a large flat plate in the NTF. Floating element balances as well as other types of skin friction measuring devices will also be tested for comparison. The surface finish will be carefully controlled and extensive boundary-layer profile surveys will be conducted. The result will be for a boundary layer much better understood than the test section sidewall cases just discussed.

The basic feasibiliy of the UTSI balance to operate in cryogenic conditions has been demonstrated, but carefully controlled testing is required to establish limits on accuracy. Work to be undertaken in the near future will include the use of fiber optics to read the movement of the belt rather than strain gages. A bench setup using fiber optics is described in reference 36. This

technique is expected to be less sensitive to temperature changes, thus simplifying balance calibration and use at cryogenic temperatures. Also electrical noise and error due to gage heat will be eliminated. Finally, eliminating the strain gage removes the primary barrier to miniaturization.

A concurrent effort is also under way to fabricate these balances using the relatively new wire-cut method (electron discharge machining using a wire for an electrode). The use of the wire-cut technique has the potential to lower the cost of the balances by reducing the part count and simplifying the assembly procedure. This technique also enhances miniaturization. The combination of the wire-cut technique and the use of fiber optics may significantly reduce the cost per balance. Reference 37 speculates on the installation of many balances on a single airfoil configuration. A typical layout is shown in figure 54 on a 14-percent thick, 10-inch chord airfoil. Each balance would be contoured to match the airfoil surface. This would simplify measurement of the location of transition separation and transonic shocks.

CONCLUDING REMARKS

The quality and pace of experimental research in aerodynamics is very much dependent on the capabilities of the instrumentation available. So our pursuit of new insights into the behavior of complex fluid flows should always be accompanied by an effort to improve the accuracy and "range" of our measurements. The validity of this statement was demonstrated in a number of instances in the present paper where new or improved instrumentation were shown to provide not only more accurate results but frequently yield new truths as well. Thin-film-gage arrays and 3-D laser instrumentation are just starting to pay dividends while multiwire hot-wire anemometers are yielding data much different from "current" techniques and offering new opportunities for unsteady flow measurements. There are several new techniuqes for skin friction measurement being investigated, one example, a compact skin-friction gage, was discussed.

REFERENCES

1. Smelt, R.: The Role of Wind Tunnels in Future Aircraft Development. Florence Guggenheim Memorial Lecture. Lisbon, Portugal, September 1978.

2. Bobbitt, Percy J.: Modern Fluid Dynamics of Subsonic and Transonic Flight. AIAA Paper 80-0861, May 1980.

3. Stack, John P.; Yeaton, Robert B.; and Dagenhart, J. R.: Research in Natural Laminar Flow and Laminar-Flow Control - Predicted and Hot-Film Measured Tollmien-Schlichting Wave Characteristics. NASA CP-2487, Part 2, 1987, pp. 377-380.

4. Croom, Cynthia C.; Manuel, Gregory S.; and Stack, John P.: In-Flight Detection of Tollmien-Schlichting Instabilities in Laminar Flow. SAE Paper 871016, April 1987.

5. Rubesin, M. W.; Okuno, A. T.; Mateer, G. G.; and Brosh, A.: A Hot-Wire Surface Gage for Skin Friction Measurements and Separation Detection. NASA TMX 62-465, 1975.

6. Harvey, W. D.; Stainback, P. C.; and Owen, F. K.: Evaluation of Flow Quality in Two Large Wind Tunnels at Transonic Speeds. NASA TP-1737, December 1980.

7. Bobbitt, P. J.; Waggoner, E. G.; Harvey, W. D.; and Dagenhart, J. R.: A Faster "Transition" to Laminar Flow. SAE Paper 851855, 1985.

8. Johnson, C. B.; Carraway, D. L.; Stainback, P. C.; and Fancher, M. F.: A Transition Detection Study Using a Cryogenic Hot Film System in the Langley 0.3-Meter Transonic Cryogenic Tunnel. AIAA Paper 87-0049, January 1987.

9. Johnson, Charles B.; Carraway, Debra L.; Hopson, Purnell, Jr.; and Tran, Sang Q.: Status of a Specialized Boundary Layer Transition Detection System for Use in the U.S. National Transonic Facility. Presented at the 12th International Congress on Instrumentation in Aerospace Simulation Facilities, Williamsburg, Virginia, June 22-25, 1987.

10. Stack, J. P.; Mangalam, S. M.; and Berry, S. A.: A Unique Measurement Technique to Study Laminar-Separation Bubble Characteristis on an Airfoil. AIAA Paper 87-1271, June 1987.

11. Stack, John P.; Mangalam, Siva M.; and Kalburgi, Vijay: The Phase Reversal Phenomenon at Flow Separation and Reattachment. AIAA Paper 88-0408, January 11-14, 1988.

12. Spangenberg, W. G.: Heat-Loss Characteristics of Hot-Wire Anemometers at Various Densities in Transonic and Supersonic Flow. NACA TN-3381, May 1955.

13. Winovich, W.; and Stine, H. A.: Measurement of the Nonlinear Variation with Temperature of Heat-Transfer Rate from Hot Wires in Transonic and Supersonic Flow: NACA TN-3965, April 1957.

14. Lowell, H. H.: Design and Applications of Hot-Wire Anemometer for Steady-State Measurements at Transonic and Supersonic Airspeed. NASA TN-2117, 1950.

15. Baldwin, L. V.: Slip-Flow Heat Transfer from Cylinders in Subsonic Airstream. NACA TN-4369, September 1958.

16. Laurence, J. C.; and Lander, L. G.: Auxiliary Equipment and Techniques for Adapting the Constant-Temperature Hot-Wire Anemometer to Specific Problems in Air-Flow Measurements. NACA TN-2843, 1952.

17. Sanborn, V. A.; and Laurence, J. C.: Heat Loss from Yawed Hot Wires at Subsonic Mach Numbers. NACA TN-3563, 1955.

18. Rose, W. C.; and McDaid, E. P.: Turbulence Measurements in Transonic Flow. AIAA 9th Aerodynamic Testing Conference, Arlington, Texas, June 7-9, 1976, pp. 267-271.

19. Horstman, C. C.; and Rose, W. C.: Hot Wire Anemometery in Transonic Flow. AIAA Journal, Vol. 15, No. 3, March 1977, pp. 375-401.

20. Stainback, P. C.; Johnson, C. B.; and Basnett, C. B.: Preliminary Measurements of Velocity, Density, and Total Temperature Fluctuation in Compressible Subsonic Flow. AIAA Paper 83-0384, AIAA 21st Aerospace Sciences Meeting, Reno, Nevada, June 10-14, 1983.

21. Stainback, P. C.: A Review of Hot Wire, Anemometery in Transonic Flows. Presented at the Eleventh International Congress on Instrumentation in Aerospace Simulation Facilities, Stanford, California, August 26-28, 1985.

22. Stainback, P. C.; and Johnson, C. B.: Flow Quality Measurements in Compressible Subsonic Flows. NASA CP-2487, Part 2, pp. 345-357.

23. Yeh, Y.; and Cummins, H. Z.: Localized Fluid Flow Measurements with an He-Ne Laser Sepctrameter Applied Physics. Letters, Vol. 4, pp. 176-178, May 1964.

24. Scheiman, J.; and Kubendian, L. R.: Juncture Flow Measurements Using Laser Velocimetry. AIAA Paper 85-1612.

25. Meyers, James F.; and Hepner, Timothy E.: Velocity Vector Analysis of a Juncture Flow Using a Three Component Laser Velocimeter. Second International Symposium on Application of Laser Anemometry to Fluid Mechanics, Lisbon, July 1984.

26. Meyers, James F.: The Elusive Third Component. Proceedings of the Symposium on Laser Anamometery, ASME 1985 Winter Annual Meeting, Miami, Florida, November 1985, pp. 247-254.

27. Scheiman, J.; and Kubendran, L. R.: Laser Velocimeter Measurements in a Wing-Fuselage Type Juncture. NASA TM-100588, April 1988.

28. Mangalam, S. M.; Dagenhart, J. R.; Hepner, T. E.; and Meyers, J. F.: The GortlerInstability on an Airfoil. AIAA Paper 85-0491, January 1985.

29. Floryan, J. M.: Stability of Boundary-Layer Flows Over Curved Walls. Ph.D. Thesis, Virginia Polytechnic Institute and State University, Blacksburg, Virginia, January 1980.

30. Jones, G. S.; Gartrell, L. R.; Sewall, W. G.; and Stainback, P. C.: Designing Transonic Wind-Tunnel Test Sections for Flow Diagnostics and Laser Velocimeter Applications. AIAA Paper 87-1434, June 1987.

31. Azzazy, M; Modarress, D.; and Hall, R.: Optical Boundary-Layer Transition Detection in a Transonic Wind Tunnel. AIAA Paper 87-1430, June 1987.

32. Dougherty, N. Sam, Jr.: Influence of Wind Tunnel Noise on the Location of Boundary-Layer Transition on a Slender Cone at Mach Numbers from 0.2 to 5.5. Volume I: Experimental Methods and Summary of Results. AEDC-TR-78-44, March 1980.

33. Vakili, A. D.; and Wu, J. M.: A New Instrument for Direct Measurement of Wall Shear Stress. Proceedings of the 28th International Instrumentation Symposium, Instrument Society of America, Vol. 19, part one, pp. 147-152, May 1982.

34. White, Frank M.: Viscous Fluid Flow. McGraw Hill Book Company, 1974.

35. Vakili, A. D.; Wu, J. M.; and Lawing, Pierce L.: Wall Shear Stress Measurements Using A New Transducer. AIAA Paper 86-1092, May 1986.

36. Vakili, A. D.; and Wu, J.M.: Direct Measurement of Skin Friction with a New Instrument. Proceedings of the Interational Symposium of Fluid Control and Measurement, Tokoyo, Japan, paper no. F43, FLUCOME 85, Pergammon Press, 1985.

37. Lawing, Pierce L.; Vakili, A. D.; and Wu, J. M.: Experience at LaRC with a UTSI Skin Friction Balance. Symposium on Natural Laminar Flow and Laminar Flow Control Research. Langley Research Center, Hampton, Virginia, March 16-19, 1987.

ACKNOWLEDGMENTS

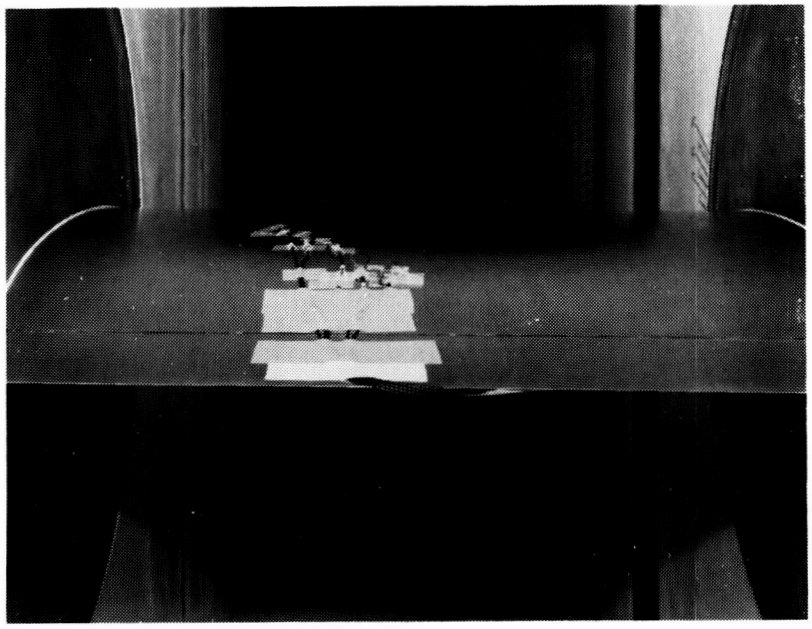
The author gratefully acknowledges the beneficial discussions with, and material obtained from, the following individuals of the Langley Research Center Staff: Charles D. Harris, William D. Harvey, J. Pete Stack, Sivaramakrishnan M. Mangalam*, Charles B. Johnson, Debra L. Carraway, James F. Meyers, Gregory S. Jones, Luther R. Gartrell, Pierce L. Lawing, Robert M. Hall, P. Calvin Stainback**, Gary F. Erickson, Cynthia C. Lee, and Robert A. Kilgore.

* Analytical Services and Materials, Inc.
** Complere

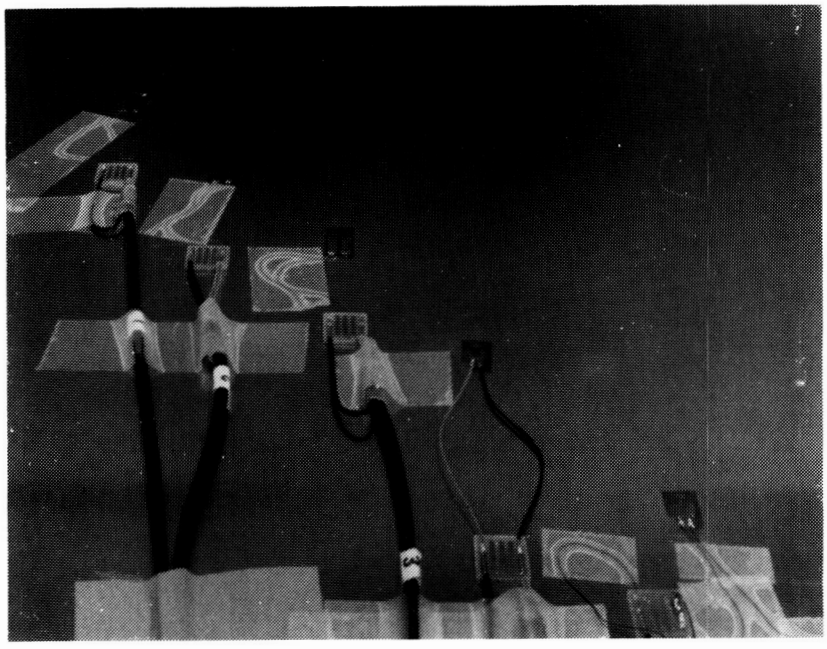
ORIGINAL PAGE IS
OF POOR QUALITY

TABLE I. - COMPARISON OF FLOW QUALITY DATA FOR 8-FOOT TPT FROM 3-WIRE AND 1-WIRE TECHNIQUES
- p_t = 710 psf, T_t = 540°R -

	3-Wire					1-Wire Method I		
Mach No.	$\tilde{u}/u$	$\tilde{\rho}/\rho$	$\tilde{T}/T_t$	$\tilde{m}/m$	$\tilde{p}/p$	$\tilde{u}/u$	$\tilde{m}/m$	$\tilde{p}/p$
0.40	0.830	0.306	0.026	0.528	0.334	0.039	0.033	0.026
0.75	2.963	0.946	0.0581	2.019	1.507	0.118	0.063	0.130
0.82	2.643	0.781	0.052	1.864	1.399	0.050	0.055	0.033



(a) Photograph of thin-film patch gages on NASA NLF(1)-0414F Airfoil installed in NASA Langley Low-Turbulence Pressure Tunnel.



(b) Enlarged photograph of patch-gage installation showing hot-film sensors and terminal blocks for anemometer leads.

Figure 1. Patch gage installation in LTPT airfoil tests.

ORIGINAL PAGE
BLACK AND WHITE PHOTOGRAPH

ORIGINAL PAGE
BLACK AND WHITE PHOTOGRAPH

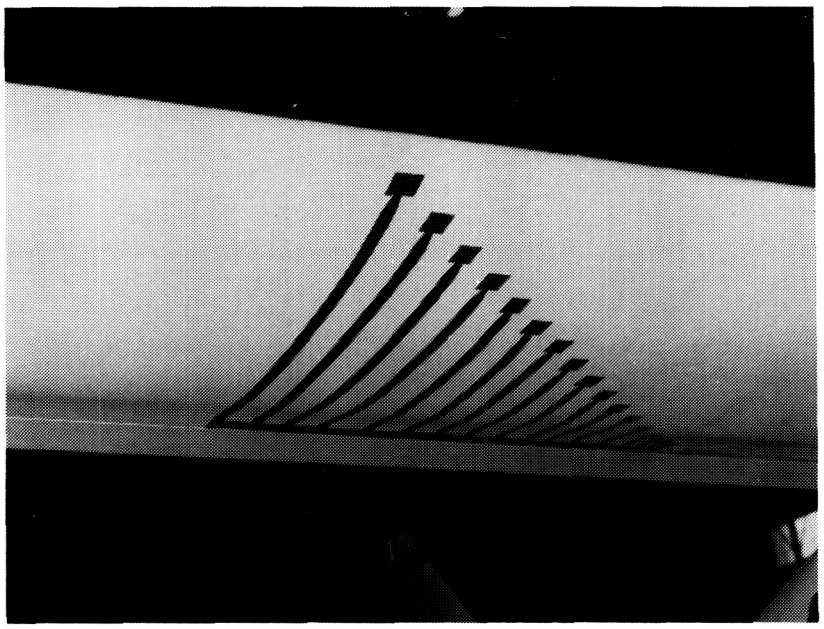


Figure 2. Photograph of an array of thin-film gages installed on the Cessna 210 with a NASA NLF(1)-0414F Airfoil glove. Photograph is taken from upstream.

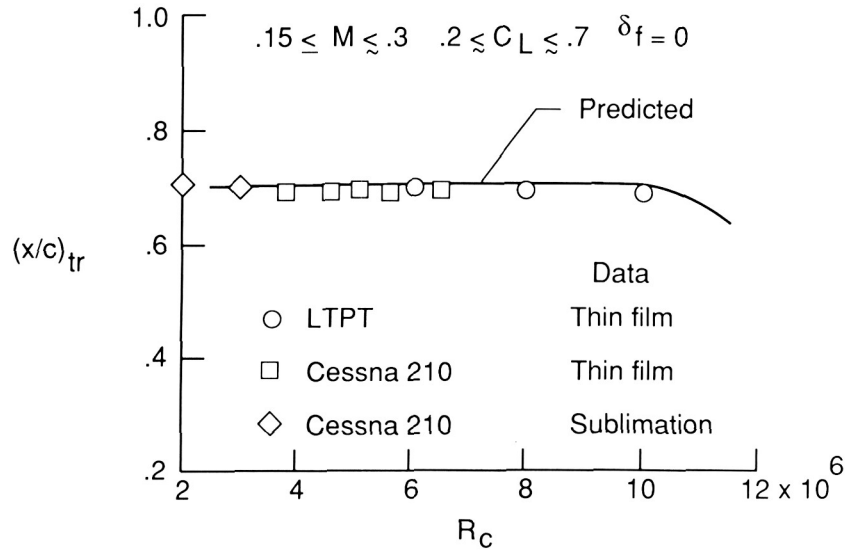


Figure 3. Comparison of wind tunnel and flight transition measurements.

ORIGINAL PAGE
BLACK AND WHITE PHOTOGRAPH

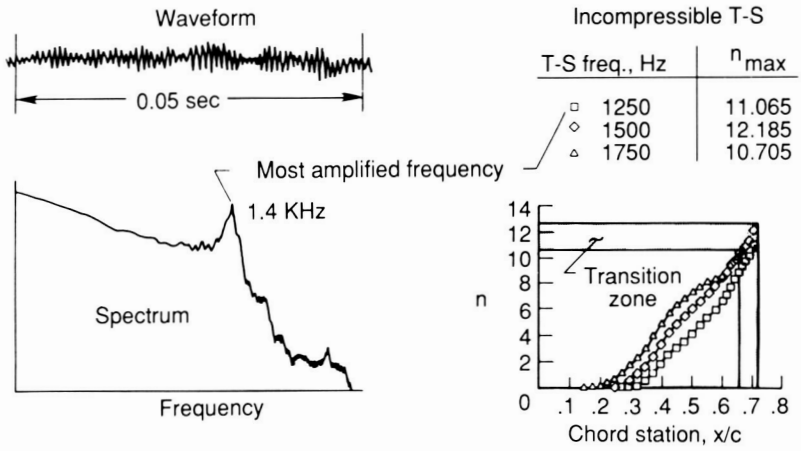


Figure 4. Predicted and measured Tollmien-Schlichting wave characteristics.

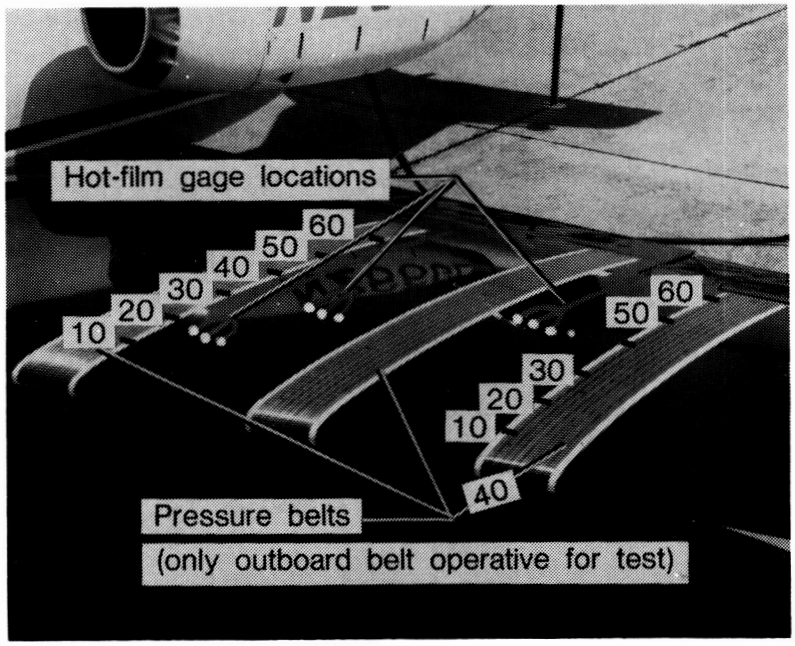


Figure 5. Lear 28/29 instrumentation for T-S instability detection test.

ORIGINAL PAGE
BLACK AND WHITE PHOTOGRAPH

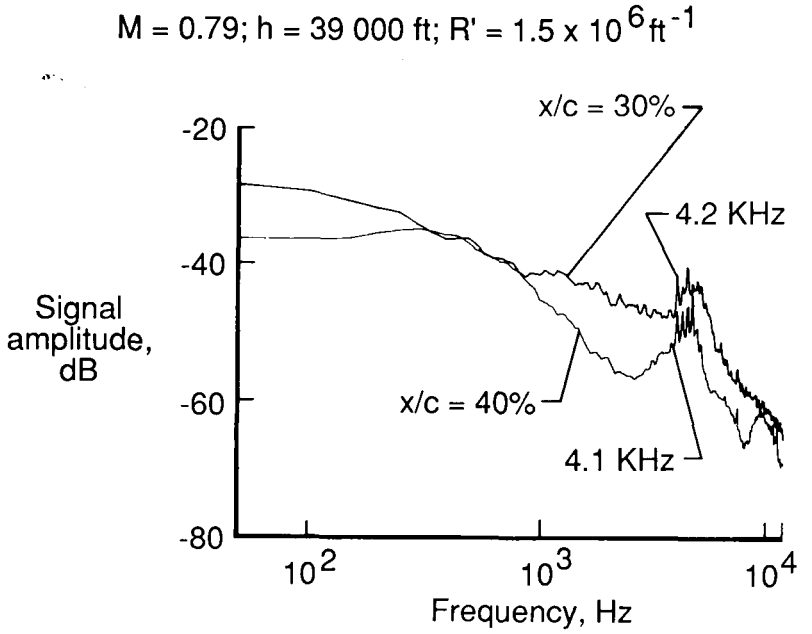


Figure 6. Power spectral density analysis of hot-film signals at 30- and 40-percent chord. M_∞ = 0.79, h = 39,000 ft, R_∞ = 1.5 x 10^6/ft.

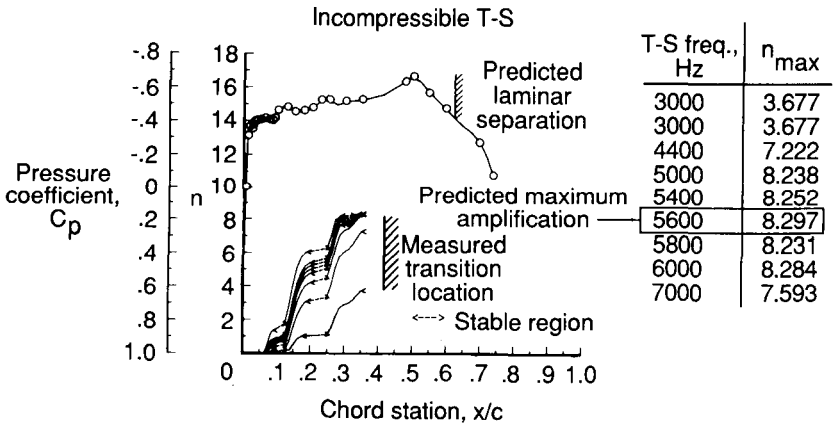


Figure 7. Incompressible prediction of T-S amplification ratios for measured pressure distribution. M_∞ = 0.79, h = 39,000 ft, R_∞ = 1.5 x 10^6/ft.

ORIGINAL PAGE
BLACK AND WHITE PHOTOGRAPH

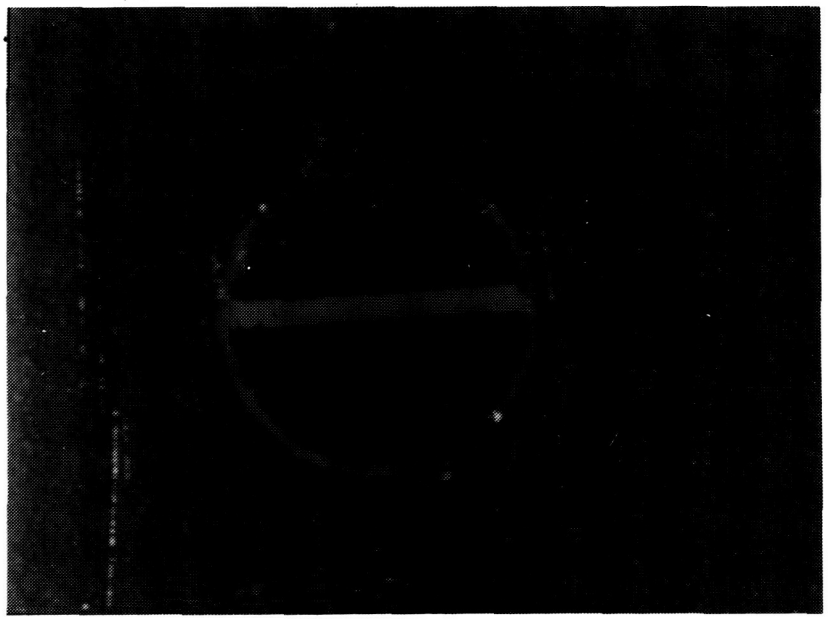


Figure 8. Enlarged photo of a thin-film plug gage installed on the 7-foot chord Laminar Flow Control (LFC) Airfoil. Diameter of plug is 0.0625 in.

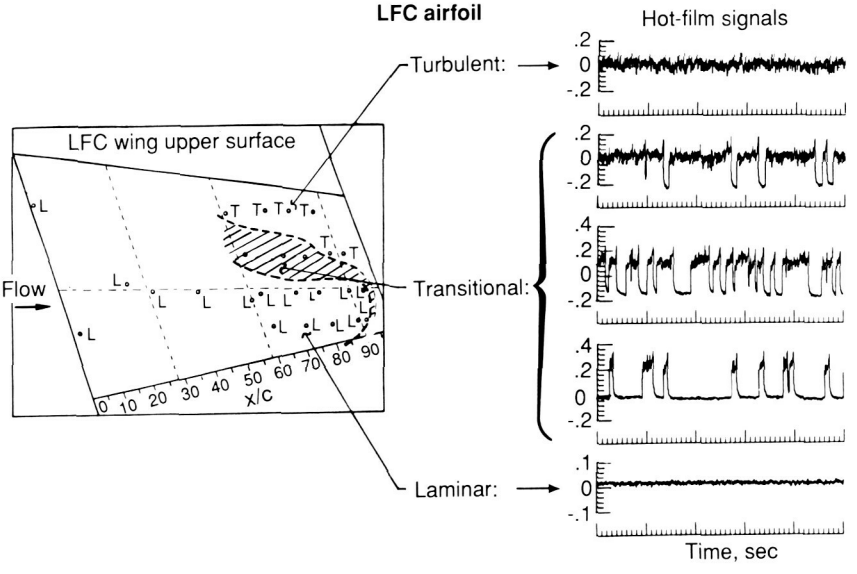


Figure 9. Sketch showing the location of the thin-film plug gages on the LFC airfoil and the state of the boundary layer at each location (L for laminar, T for turbulent).

ORIGINAL PAGE
BLACK AND WHITE PHOTOGRAPH

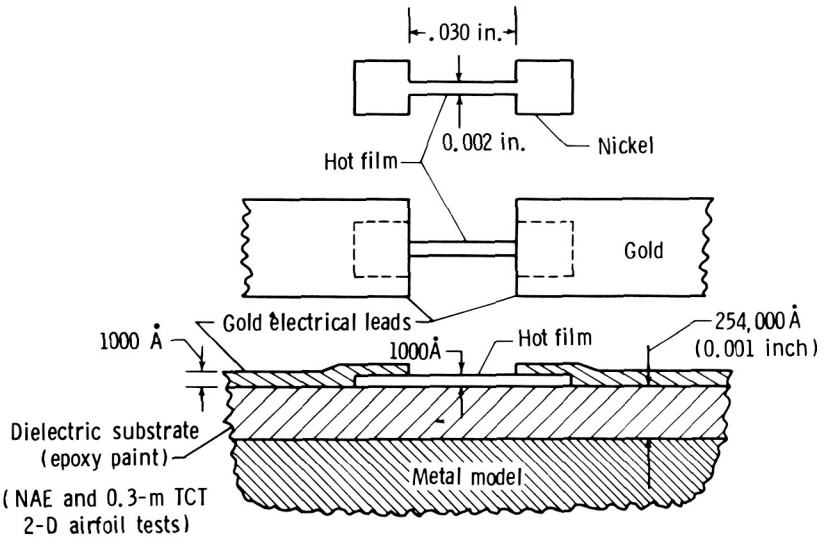


Figure 10. Sketch showing the construction of the McDonnell-Douglas hot-film gages, leads, and substrate.

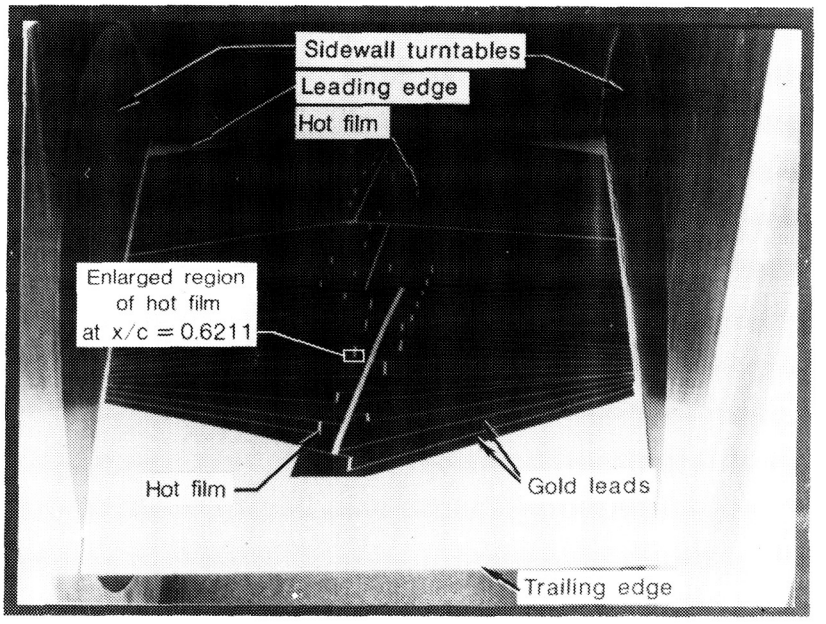
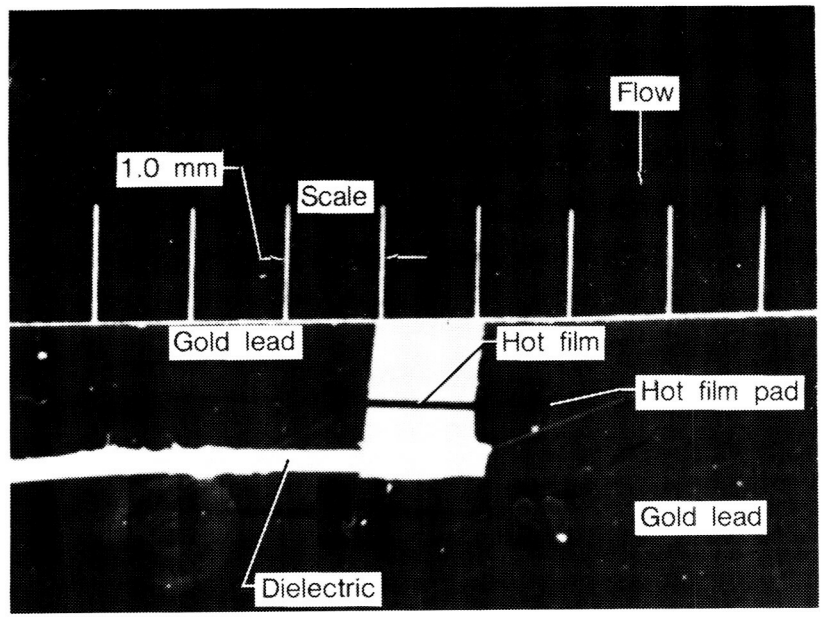


Figure 11(a). Photograph of the supercritical airfoil model installed in the 0.3-M TCT showing the vapor-deposited gold hot-film leads.



(b) Enlarged photographs of hot-film sensor, gold leads, and dielectric substrate.

Figure 11. Photographs of a supercritical airfoil model with hot-film gage installation.

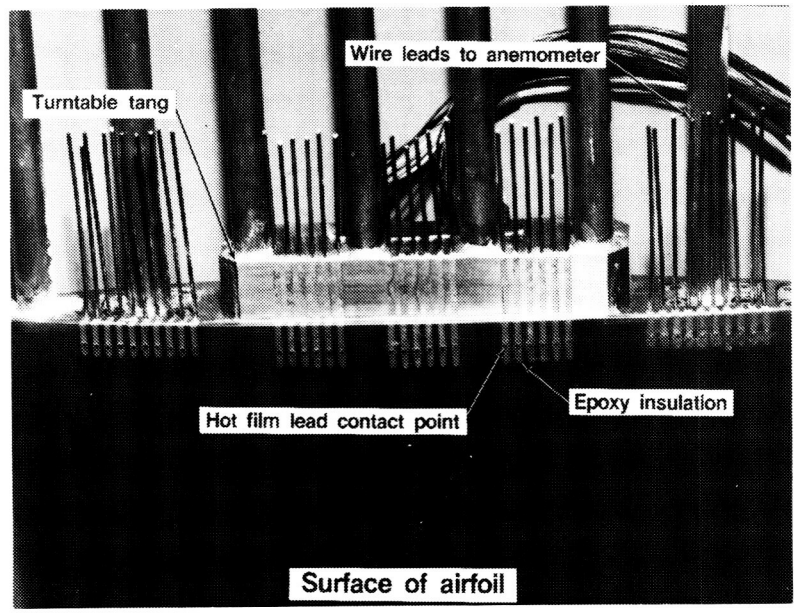
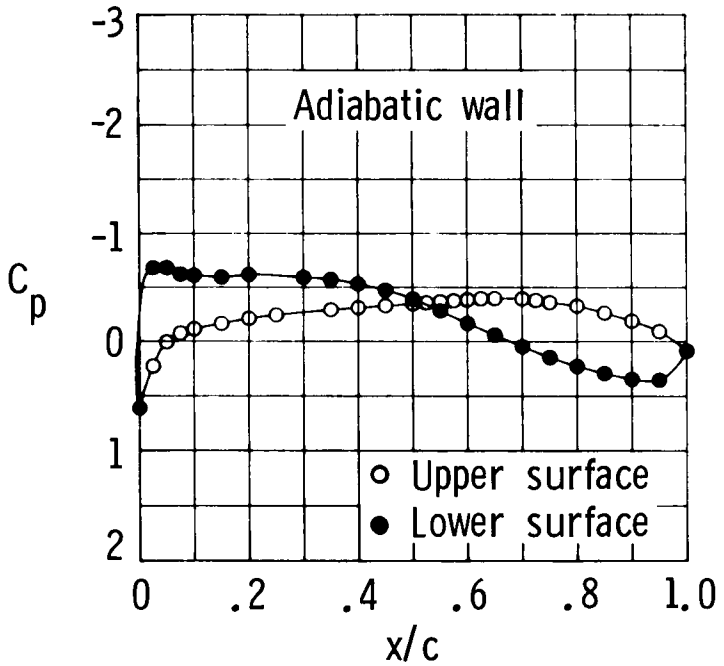
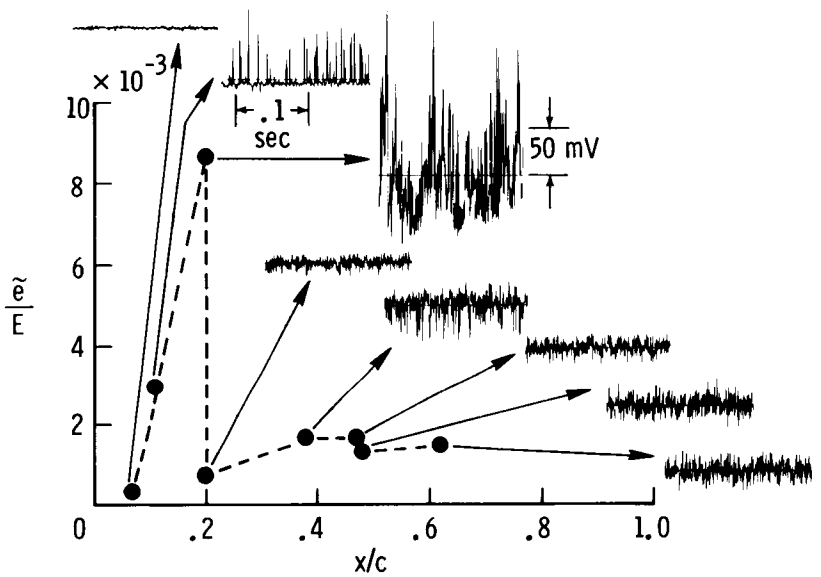


Figure 12. Photograph of end of supercritical airfoil model showing hot-film-lead contacts and anemometer leads.

ORIGINAL PAGE
BLACK AND WHITE PHOTOGRAPH



(a) Airfoil pressure distribution.



(b) Normalized RMS flucuating voltages for a number of chordwise locations.

Figure 13. A typical airfoil pressure distribution and normalized RMS flucuating voltages from the 0.3-M TCT hot film tests. Adiabatic wall, $M_\infty = 0.6$, $R_c = 7.5 \times 10^6$, $\alpha = 4.0^0$, $T_t = 360°R$.

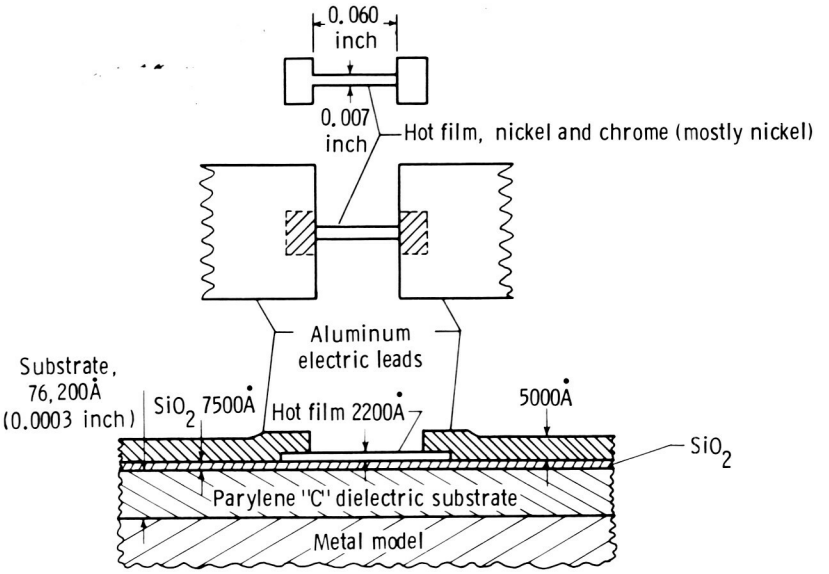


Figure 14. Sketch showing the construction of the Langley developed scheme of hot-film deposition.



Figure 15. Airfoil mounted on the sidewall of the NTF for tests of the hot-film dielectric.

ORIGINAL PAGE
BLACK AND WHITE PHOTOGRAPH

ORIGINAL PAGE
BLACK AND WHITE PHOTOGRAPH

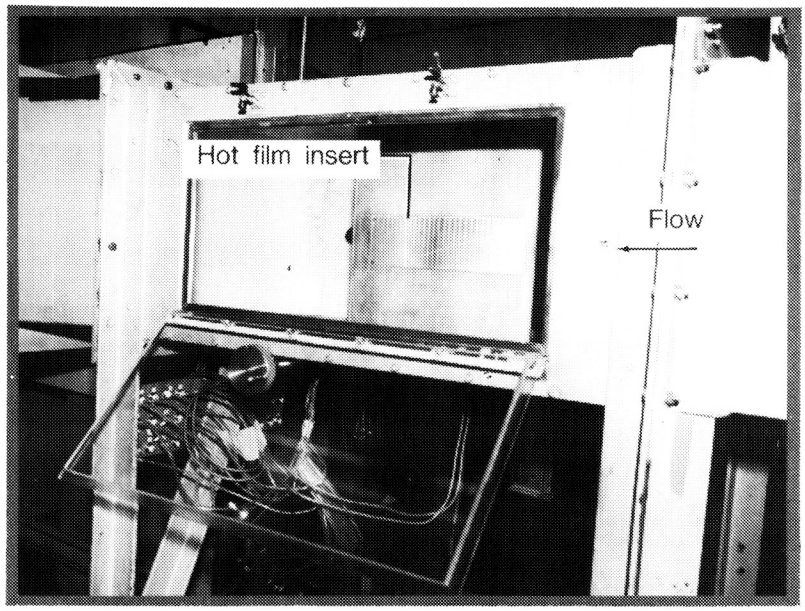


Figure 16. NACA 0012 Airfoil model installed in test section of IRD small calibration facility.

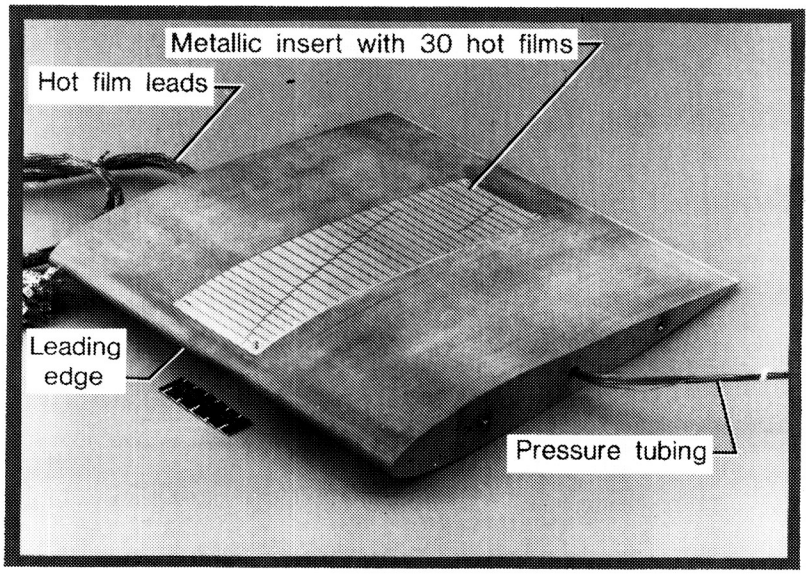


Figure 17. 2-D airfoil with hot-film insert used to demonstrate on-line transition detection with cryogenic hot-film system. NASA 0012 Airfoil c = 12 in., 12-in. span.

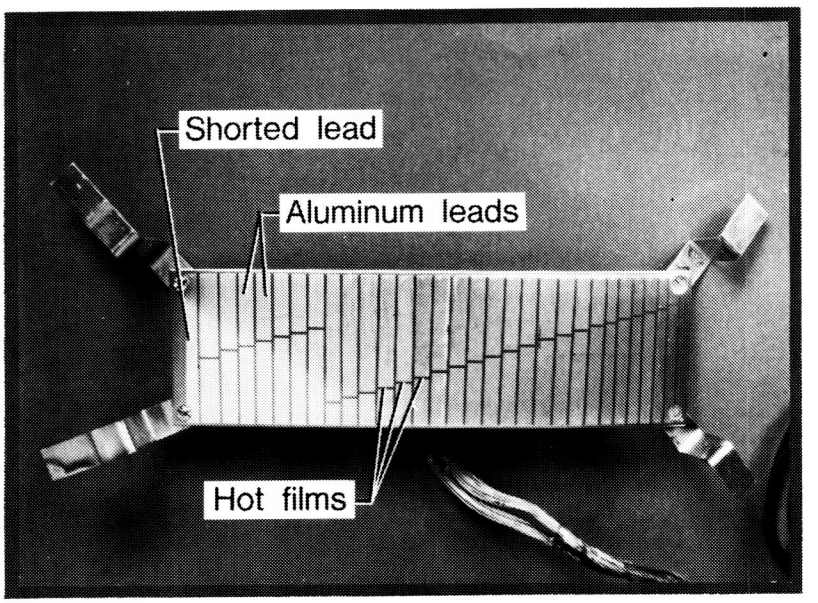


Figure 18. Metallic insert with 30 Langley developed cryogenic hot-film sensors.

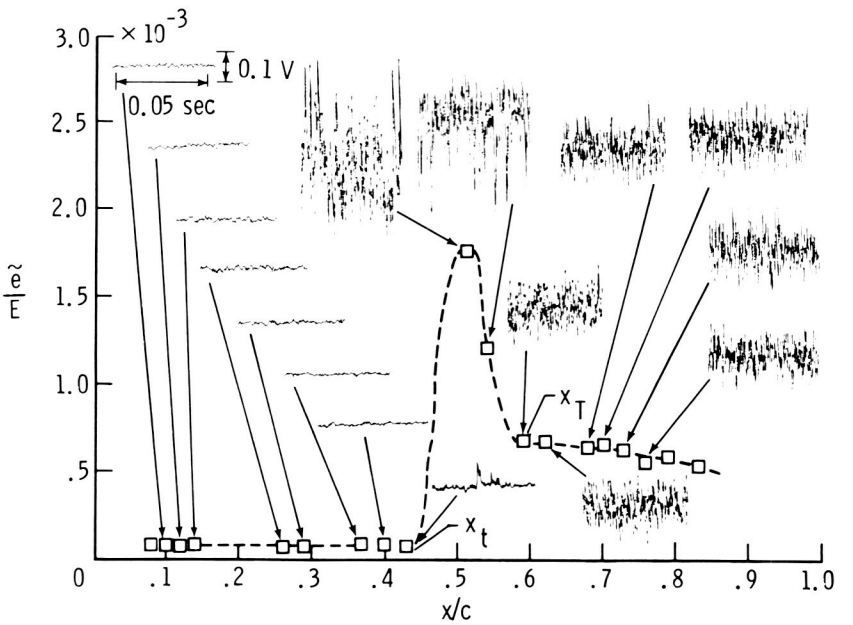


Figure 19. Normalized RMS fluctuating voltages for a number of chordwise locations. $\alpha = 0^0$, $M_\infty = 0.122$, $R_c = 0.86 \times 10^6$, $c = 12$ in.

ORIGINAL PAGE
BLACK AND WHITE PHOTOGRAPH

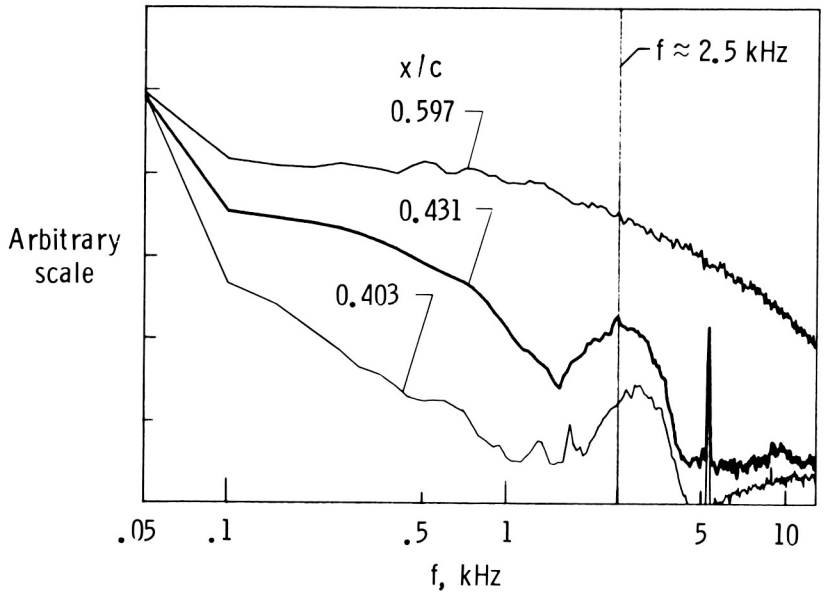


Figure 20. Spectra at three chordwise locations showing amplification of T-S waves in vicinity of 2.5 KH_z. $\alpha = 0^0$ $M_\infty = 0.122$, $R_c = 0.86 \times 10^6$.

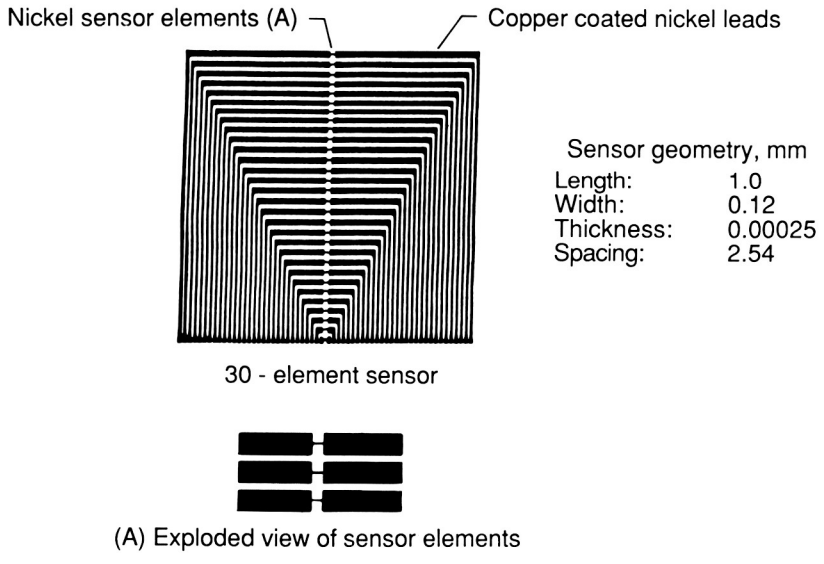


Figure 21. Prototype hot-film sensor array.

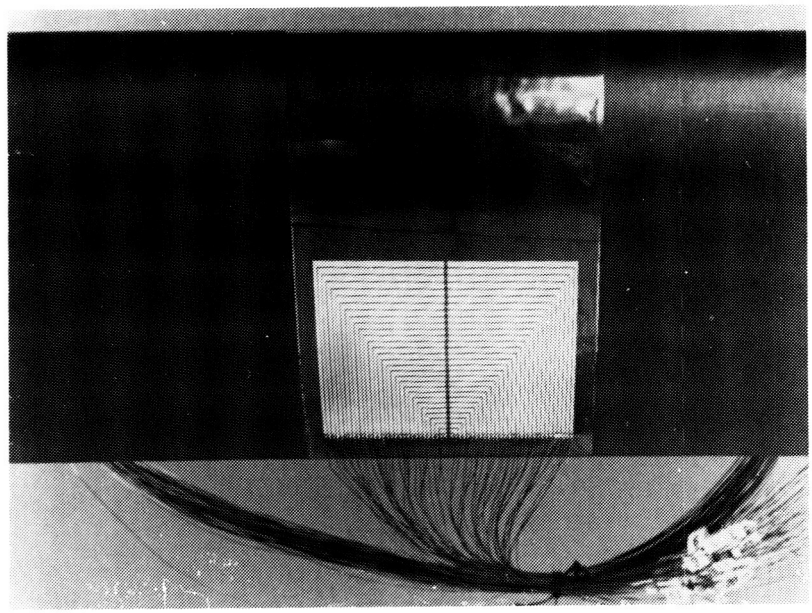


Figure 22. Photograph of prototype hot-film sensor array of polyimide substrate bonded to LRN(1)-1010 airfoil model. 15-cm chord, 30.48-cm span.

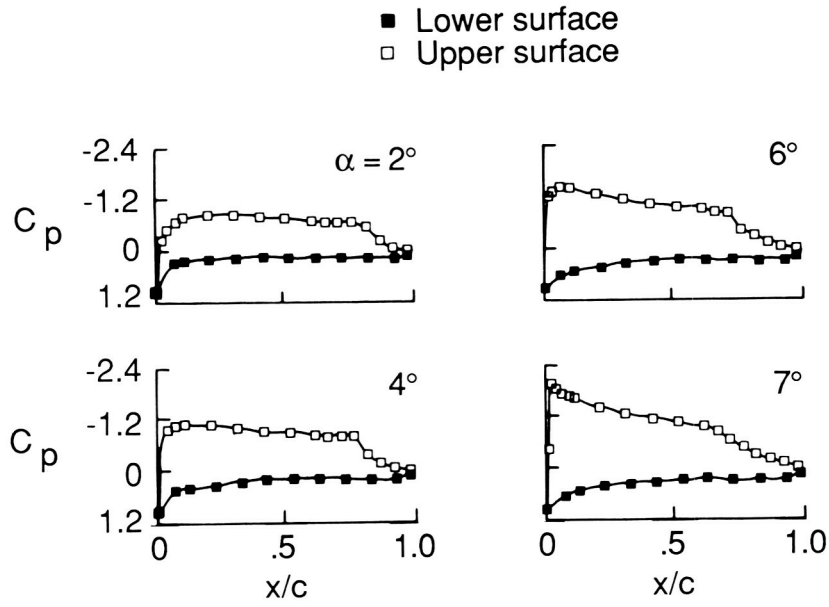


Figure 23. Pressure distribution for various angles of attack of LRN(1) 1010 airfoil. $R_c = 0.200 \times 10^6$, $M_\infty = 0.06$.

ORIGINAL PAGE
BLACK AND WHITE PHOTOGRAPH

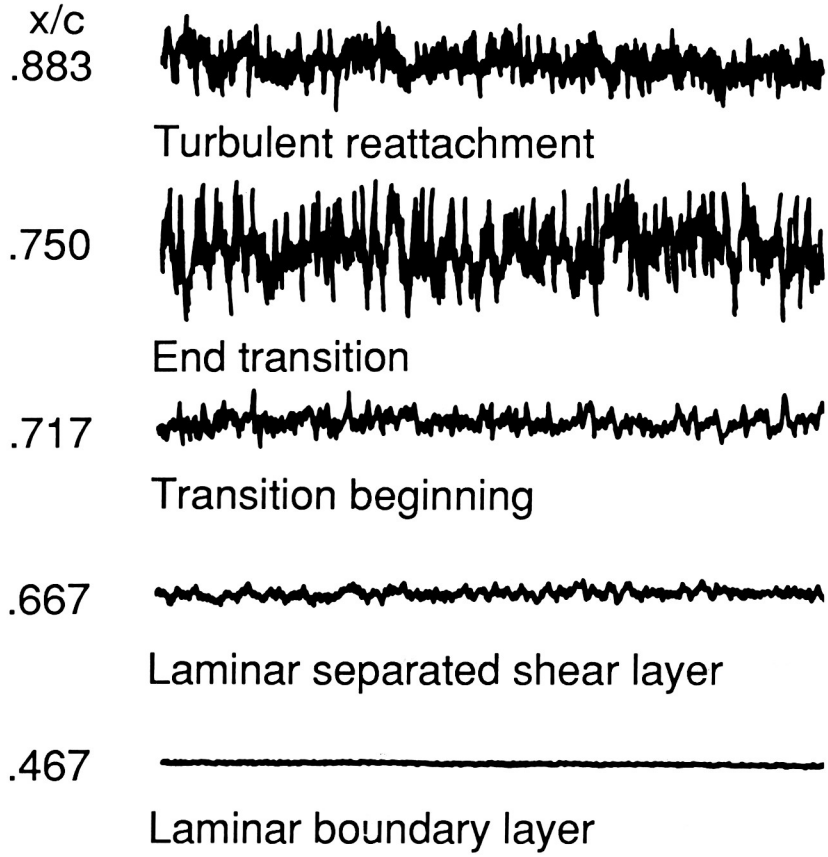


Figure 24. Time history of signals from hot films at five chord locations. R_c = 199,900, $\alpha = 5^0$, M_∞ = 0.06.

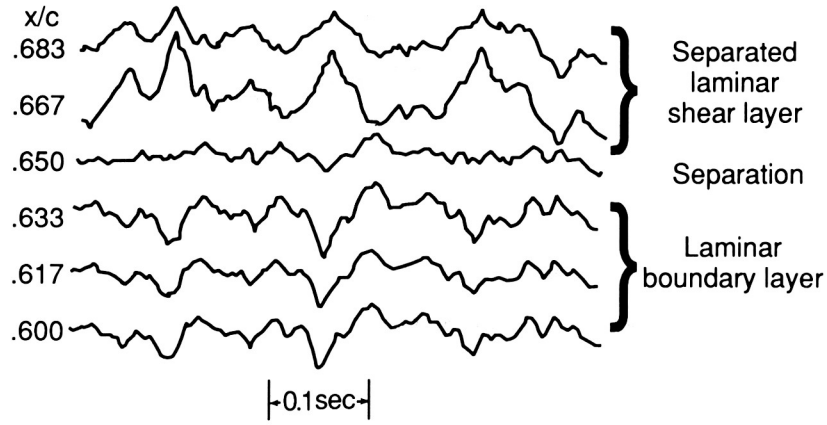


Figure 25. Time history of signals from gages in laminar separation region.

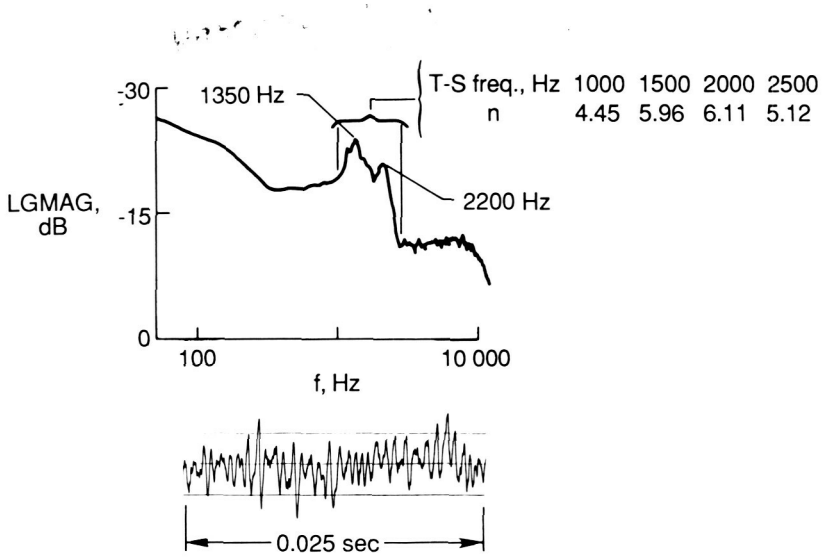


Figure 26. Auto correlation of hot-film signals and comparison of most amplified T-S frequencies with stability theory. A typical time history plot of output signal is given in the lower part of the picture. $\alpha = 7.25^0$, $R_c = 0.222 \times 10^6$, $x/c = 0.6$.

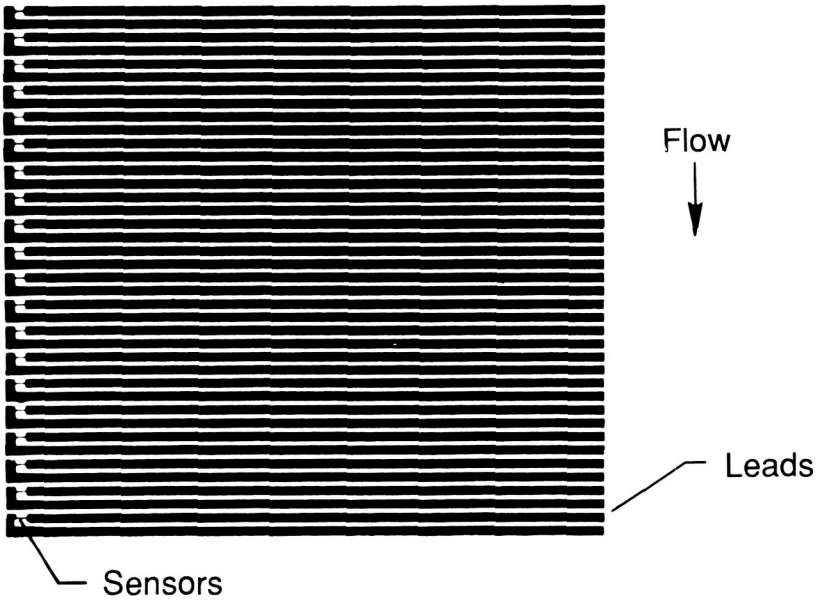


Figure 27. Improved multi-element sensor configuration.

ORIGINAL PAGE
BLACK AND WHITE PHOTOGRAPH

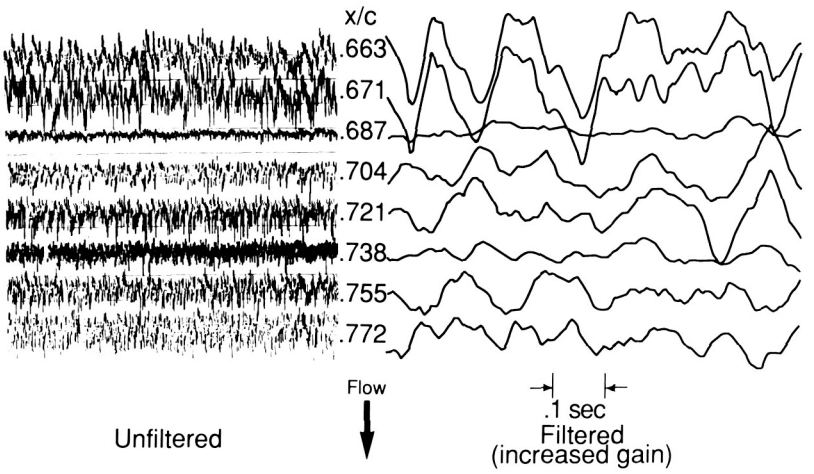


Figure 28. Time history of signals in the laminar reattachment region on Eppler-387 airfoil at R_c = 200,000, $\alpha = 2^0$, $M_\infty = 0.06$

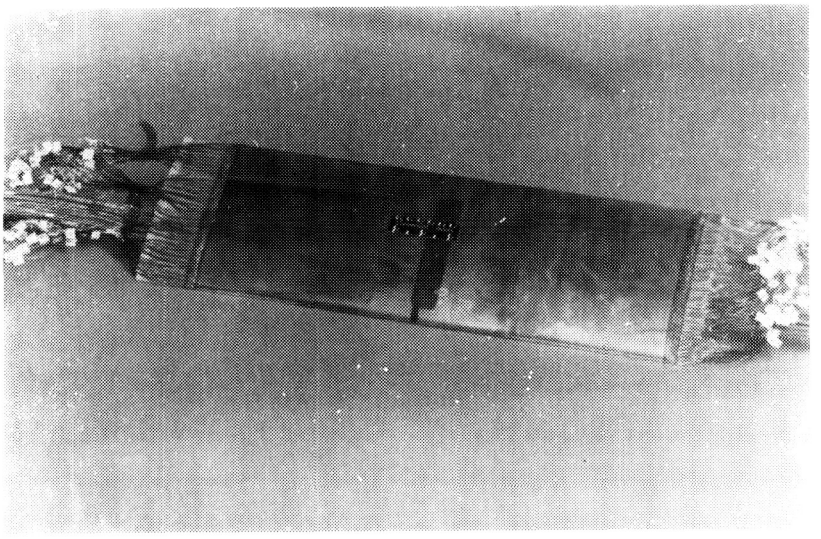
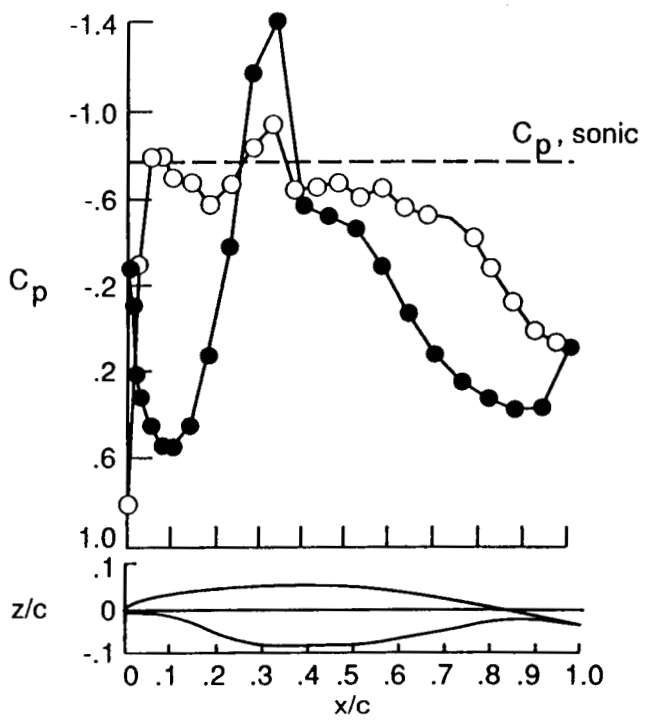


Figure 29(a). Photograph of airfoil model, with thin-film arrays bonded to the surface, that was used in the 0.3-M TCT tests.



(b) Pressure distribution on airfoil model. $\alpha = -1.02^0$, $M_\infty = 0.70$, $R_c = 6 \times 10^6$.

Figure 29. Airfoil model tested in 0.3-M TCT and an example of pressure distribution.

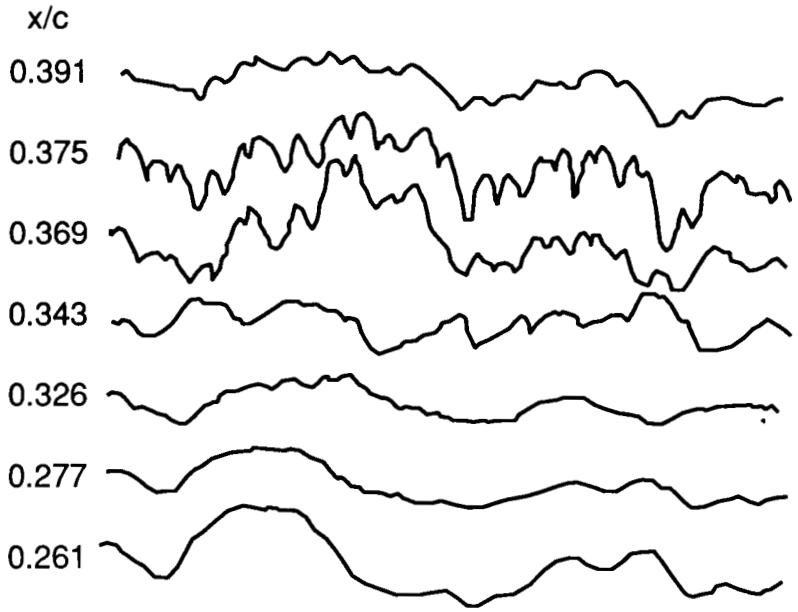


Figure 30. Time traces of voltage outputs from gages in the vicinity of shock on the lower surface of the airfoil.

ORIGINAL PAGE
BLACK AND WHITE PHOTOGRAPH

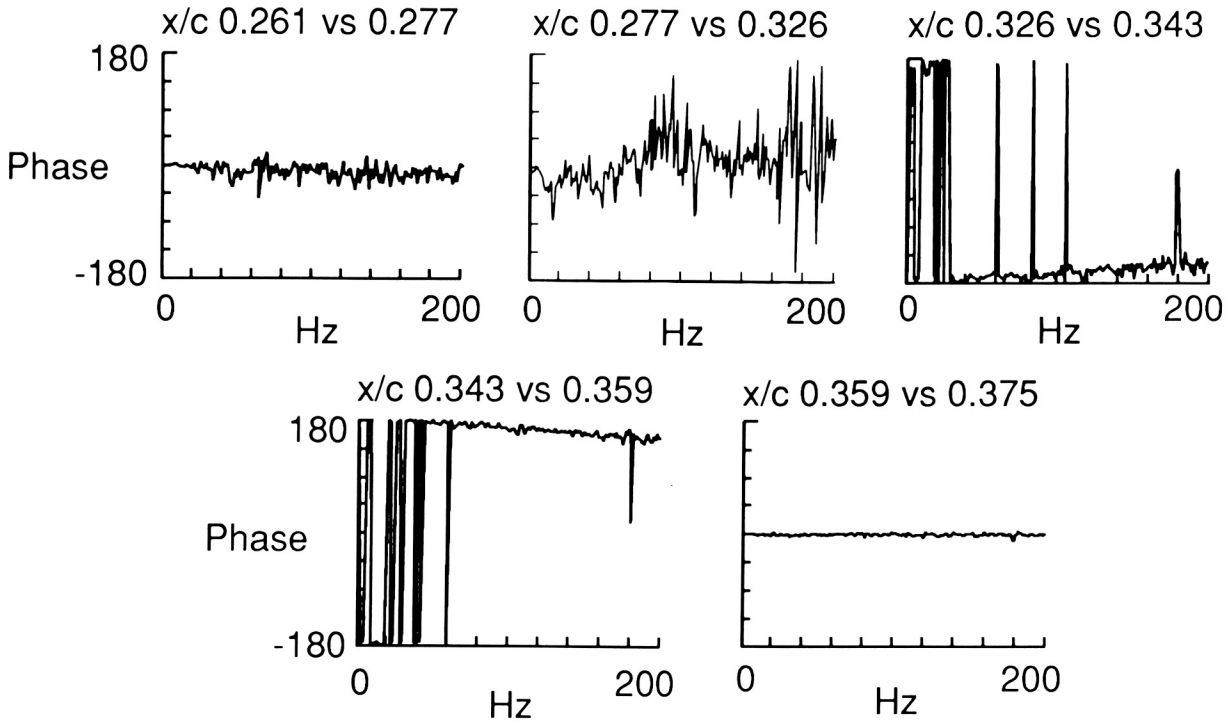


Figure 31. Phase correlation between successive gages showing phase reversals at separation and reattachment.

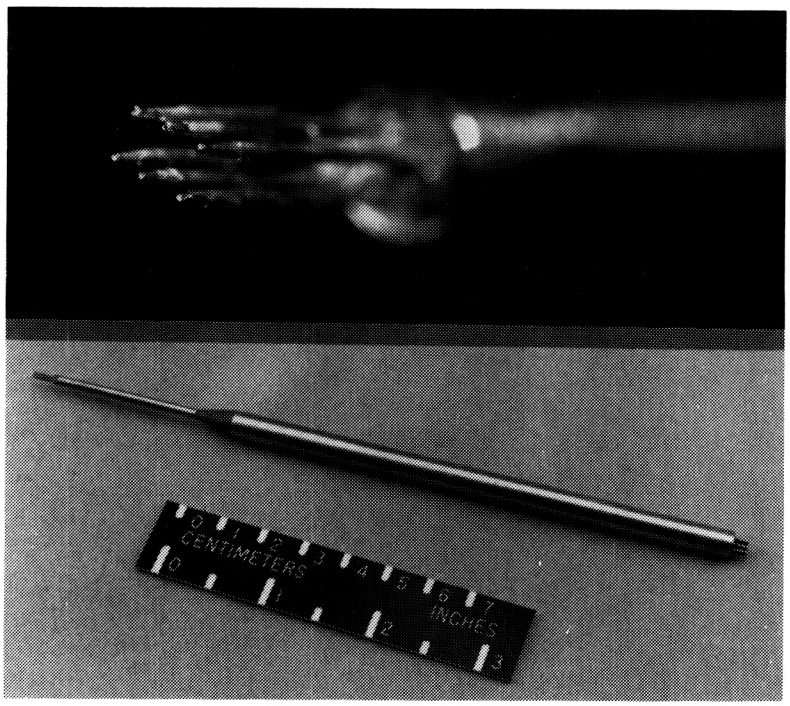


Figure 32. Enlarged photograph of a three-wire, hot-wire probe.

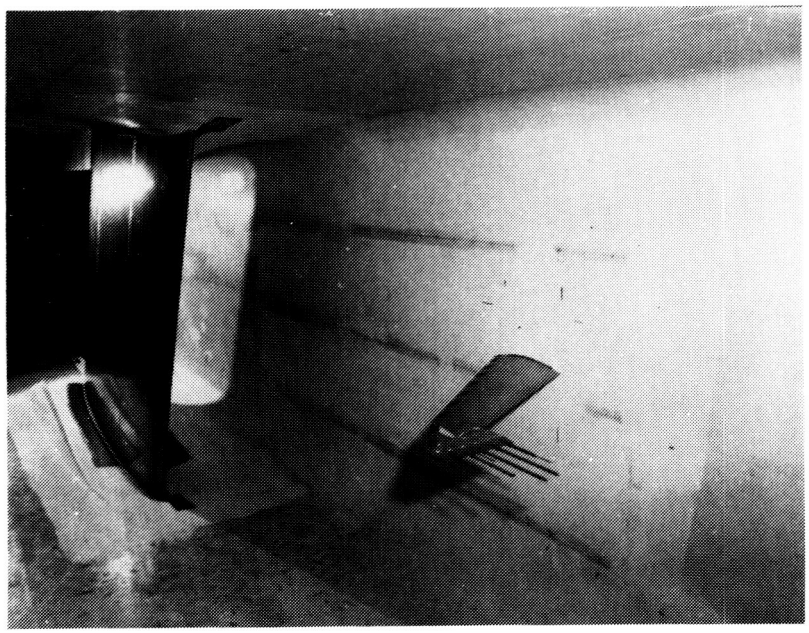
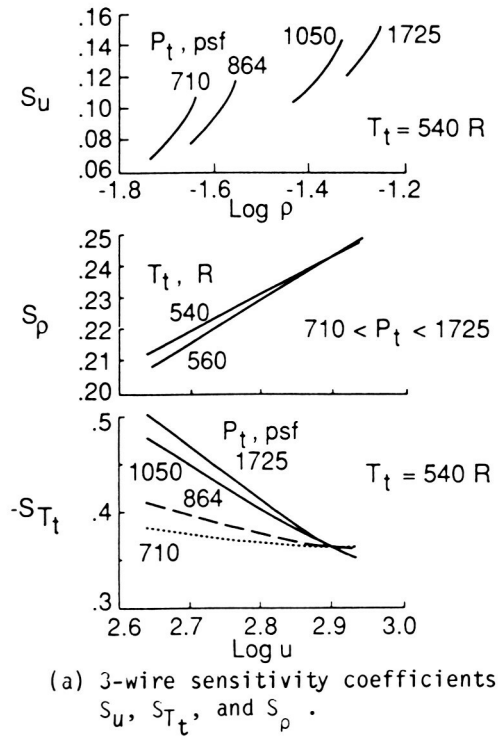
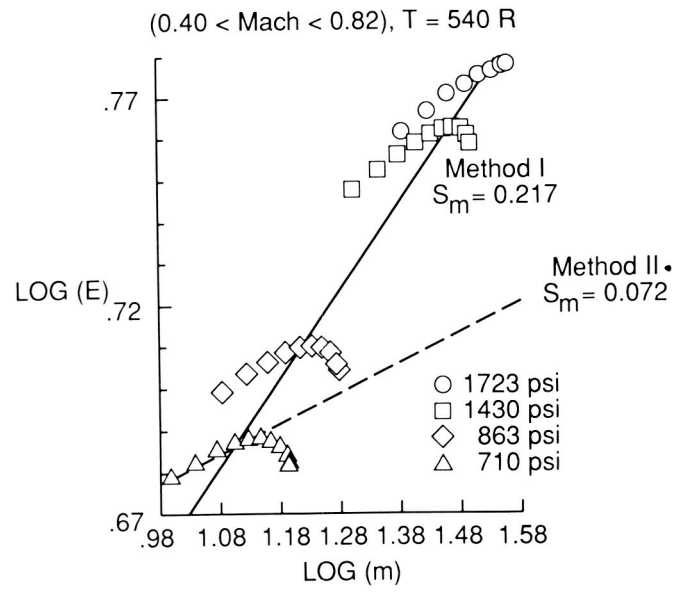


Figure 33. Photographs of probe-rake installation in LaRC 8-Foot Transonic Pressure Tunnel.



(a) 3-wire sensitivity coefficients S_u, S_{T_t}, and S_ρ.



(b) Single wire variations of log(E) with log (m) and the associated sensitivities for Method I and II.

Figure 34. Single and 3-wire sensitivity coefficients.

ORIGINAL PAGE
BLACK AND WHITE PHOTOGRAPH

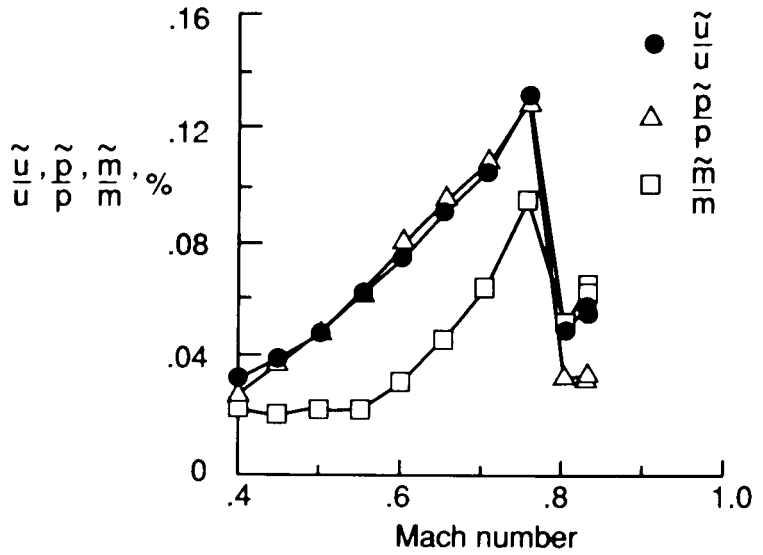


Figure 35. The variation of $\tilde{u}/u$, $\tilde{p}/p$, and $\tilde{m}/m$ with Mach number as determined from a single-wire hot-wire anemometer and microphone in the LaRC 8'TPT. p_t = 710 psf.

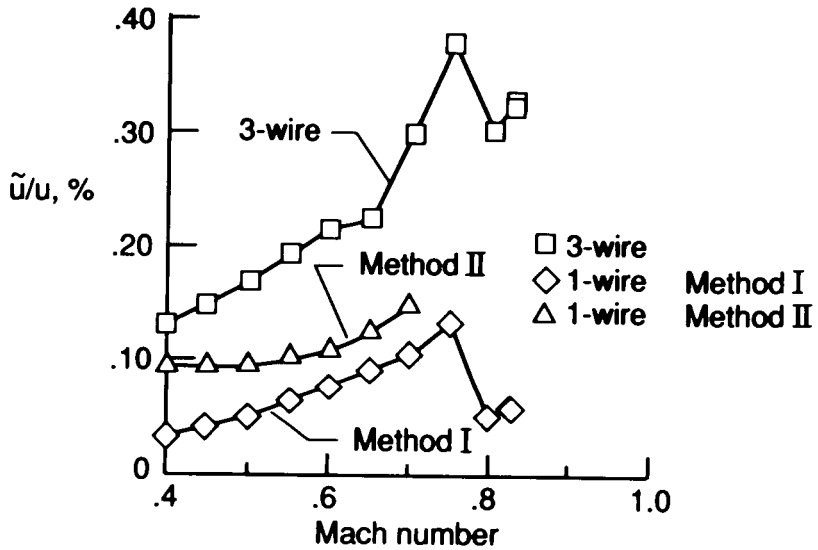


Figure 36. The variation of $\tilde{u}/u$ with Mach number for both single and 3-wire anemometers. p_t = 710 psf.

ORIGINAL PAGE
BLACK AND WHITE PHOTOGRAPH

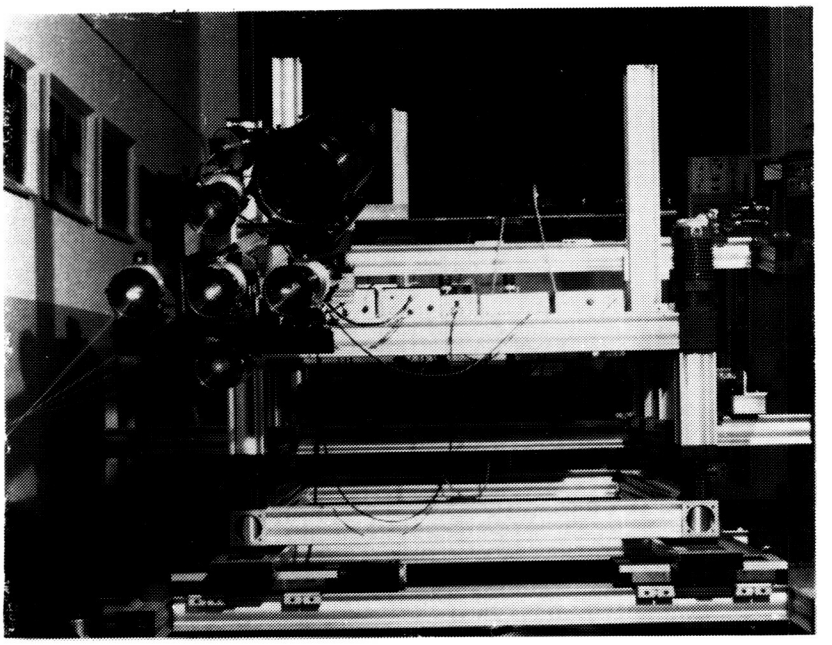


Figure 37. Photograph of the signal axis, 5-beam, 3-component LDV system used in LTPT Taylor-Gortler instability and juncture-flow investigations.

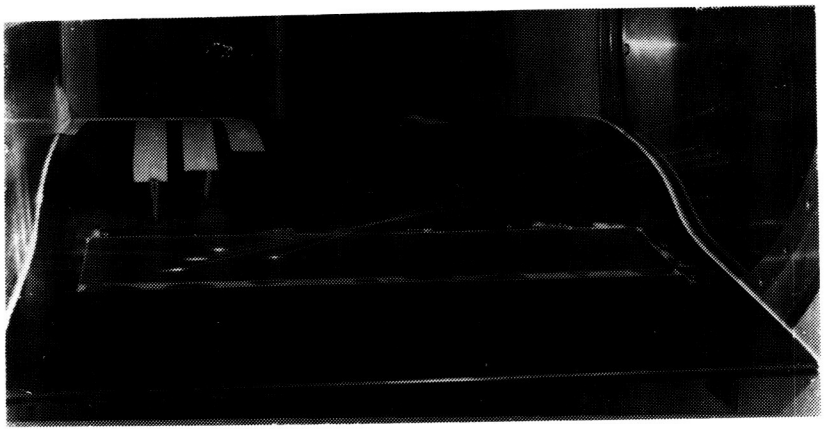


Figure 38. Photograph of airfoil with concave surface used in Taylor-Gortler instability investigation.

ORIGINAL PAGE
BLACK AND WHITE PHOTOGRAPH

ORIGINAL PAGE
COLOR PHOTOGRAPH

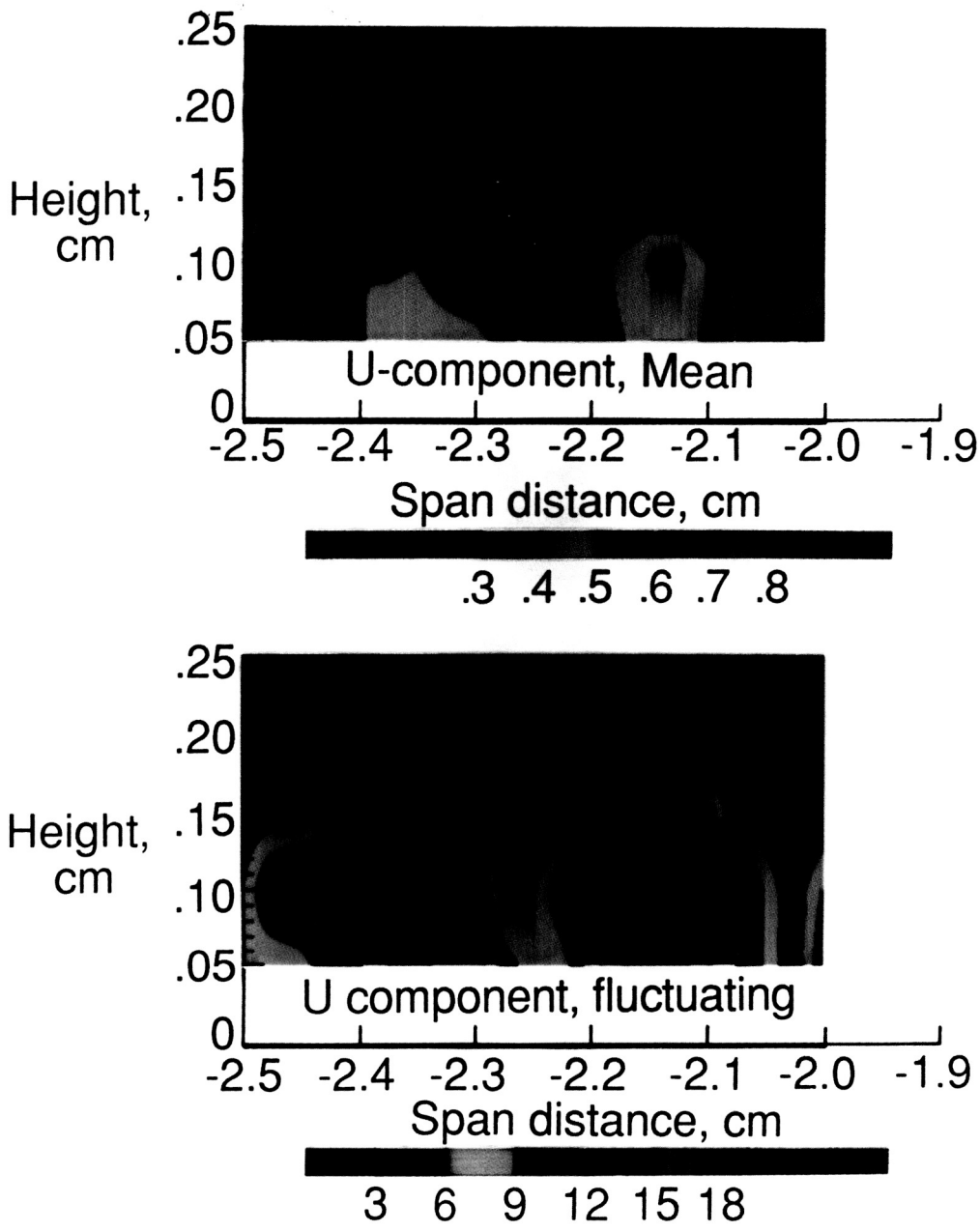


Figure 39. Contour plots of mean and fluctuating u components of velocity field obtained by 3-component LDV showing structure of Taylor-Gortler vortices.



Figure 40. Flow-visualization picture of Taylor-Gortler vortices in airfoil concave region looking downstream.

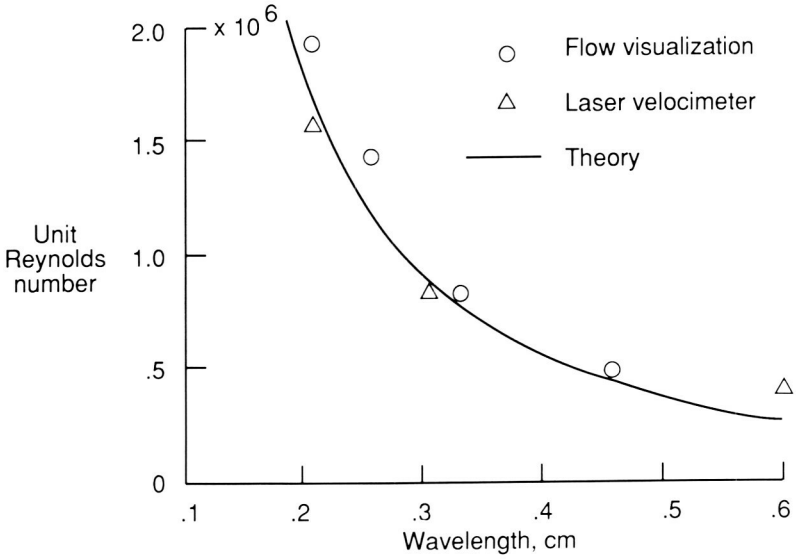


Figure 41. Comparison of theoretical and experimental data on Taylor-Gortler vortex spacing.

ORIGINAL PAGE
BLACK AND WHITE PHOTOGRAPH

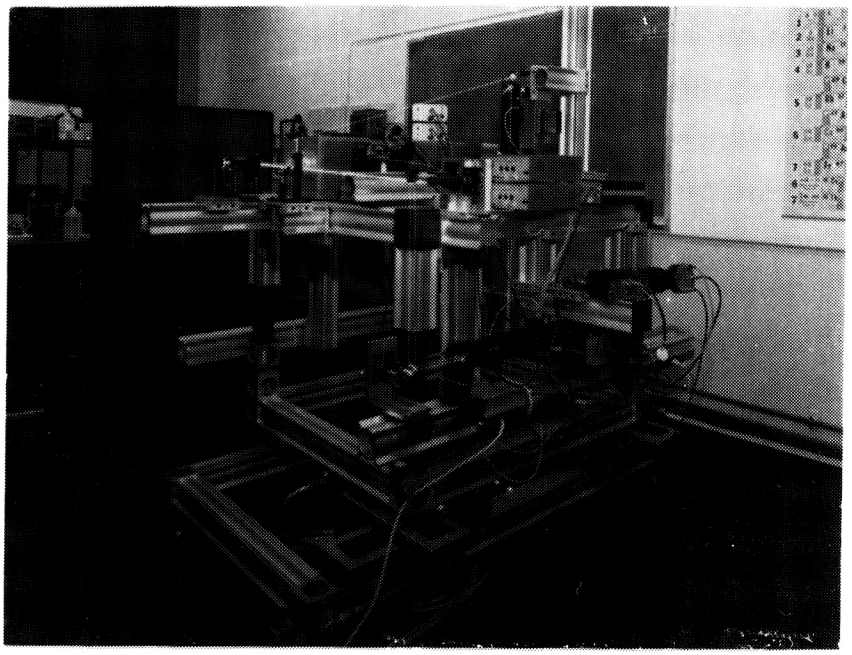


Figure 42. Photograph of orthogonal 3-component LDV system set up in laboratory to measure pipe flow.

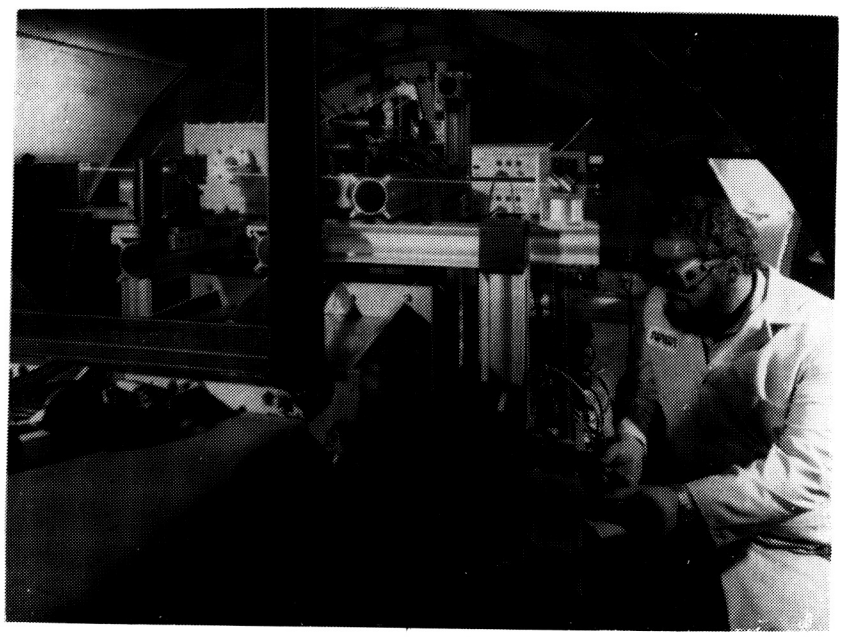
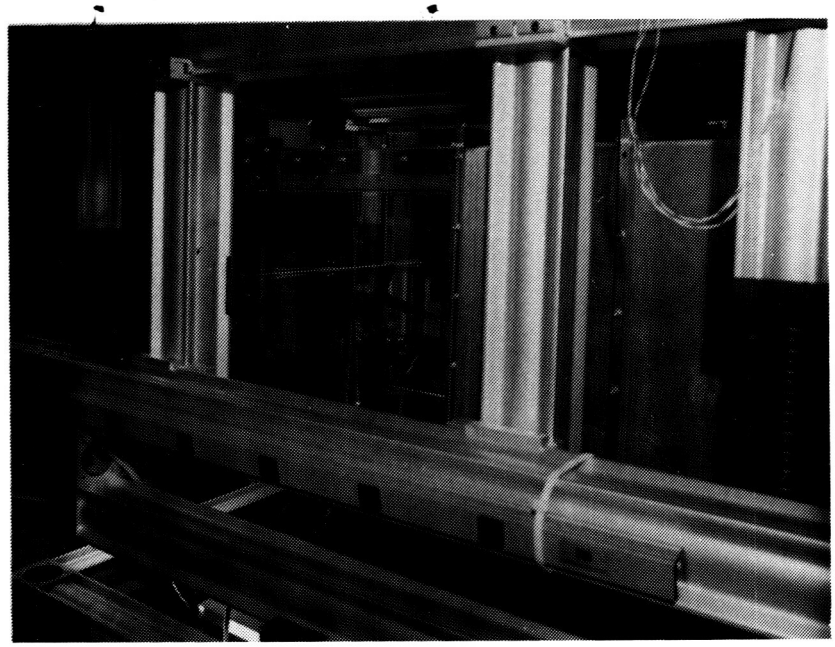
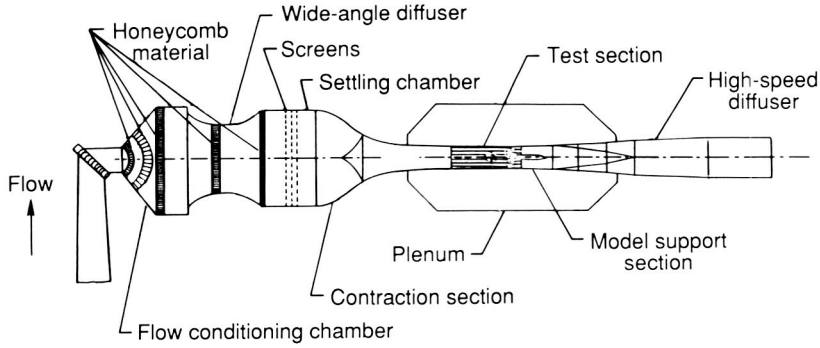


Figure 43. Photograph of an orthogonal 3-component LDV system installed in the Basic Aerodynamics Research Facility.

ORIGINAL PAGE
BLACK AND WHITE PHOTOGRAPH



(a) Photograph of glass-walled test section with wall-interference model mounted on sting.



(b) Sketch of Basic Aerodynamics Research Facility showing contraction, test-section, plenum, and high speed diffuser.

Figure 44. Features of Basic Aerodynamics Research Facility.

ORIGINAL PAGE
BLACK AND WHITE PHOTOGRAPH

ORIGINAL PAGE IS
OF POOR QUALITY

ORIGINAL PAGE
COLOR PHOTOGRAPH

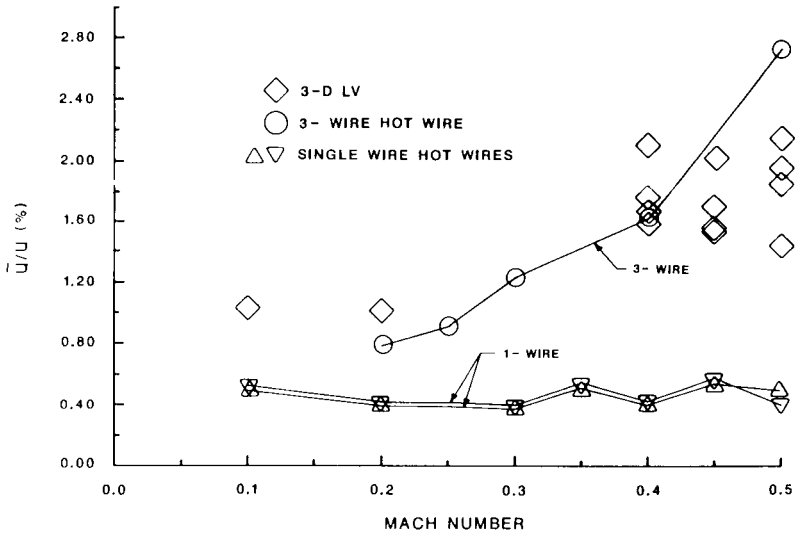


Figure 45. Comparison of hot-wire and LDV measurements for u/u in BARF.

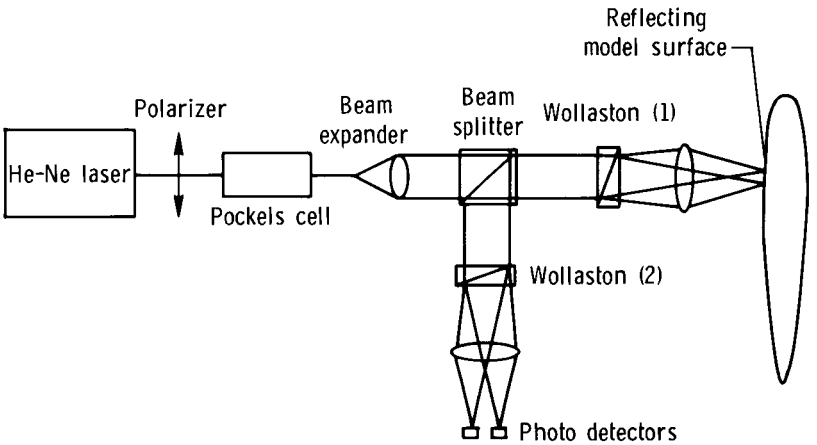


Figure 46. Schematic of laser interferometer system.

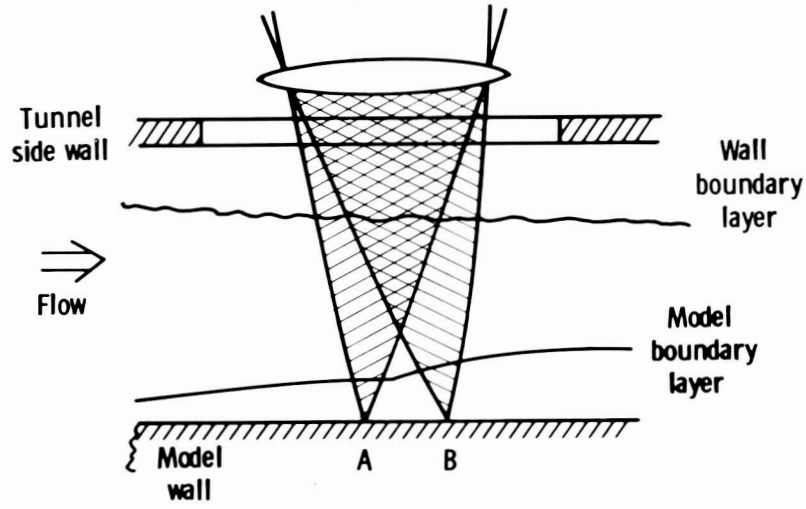


Figure 47. Sketch showing optical paths near model.

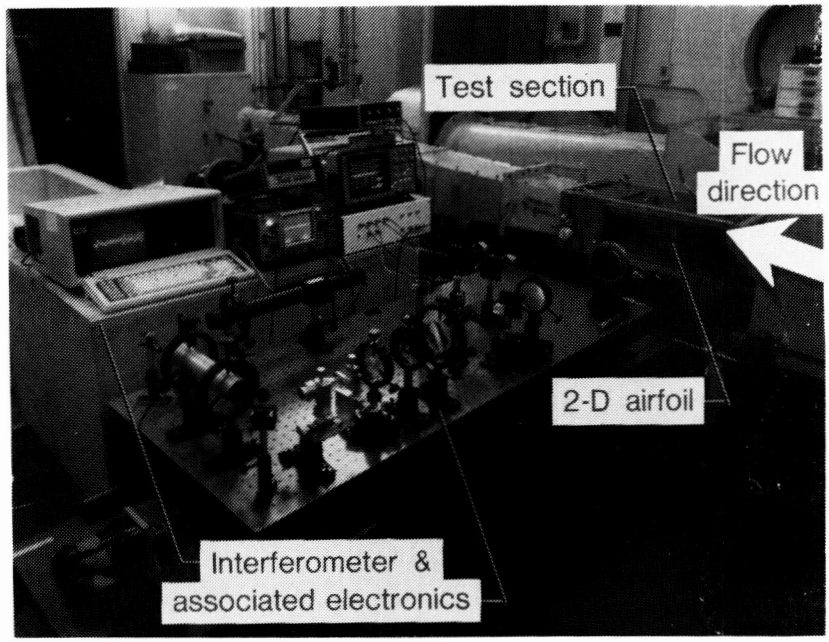
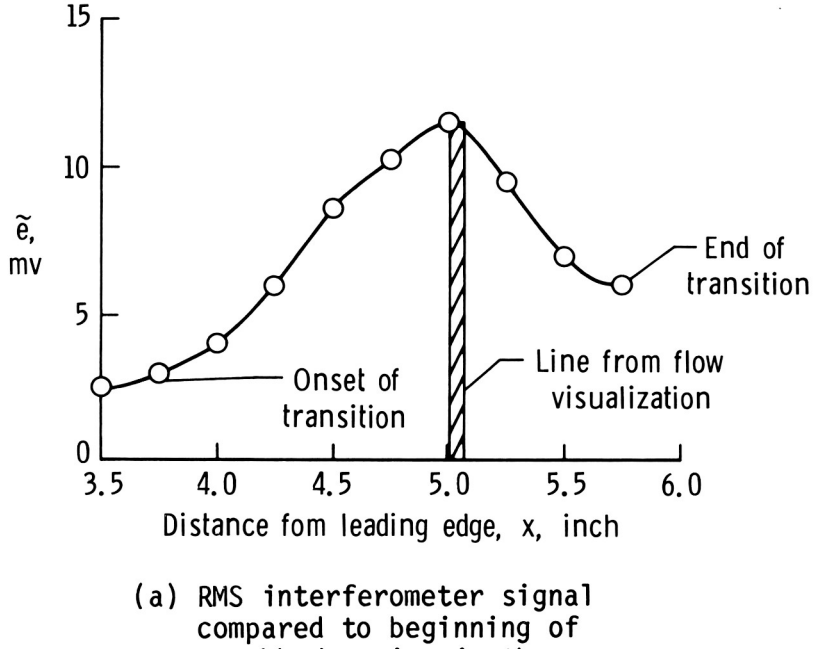


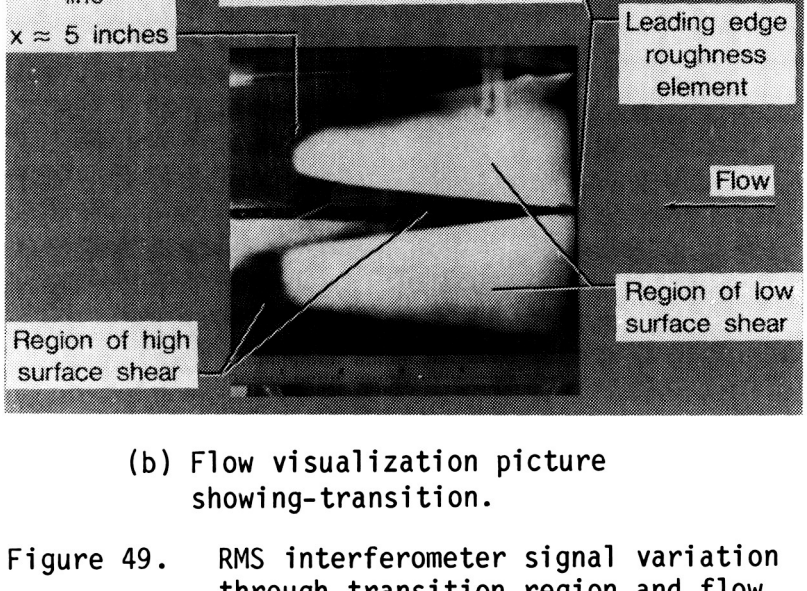
Figure 48. Photograph showing transition detection system (interferometer) installed in the Boeing Model Transonic Wind Tunnel.

ORIGINAL PAGE
BLACK AND WHITE PHOTOGRAPH

ORIGINAL PAGE
BLACK AND WHITE PHOTOGRAPH



(a) RMS interferometer signal compared to beginning of scrubbed region in the sublimating chemical flow visualization. NACA 66-066, $M_\infty = 0.70$, $R_c = 2 \times 10^6$.



(b) Flow visualization picture showing-transition.

Figure 49. RMS interferometer signal variation through transition region and flow visualization picture showing transition location.

ORIGINAL PAGE
BLACK AND WHITE PHOTOGRAPH

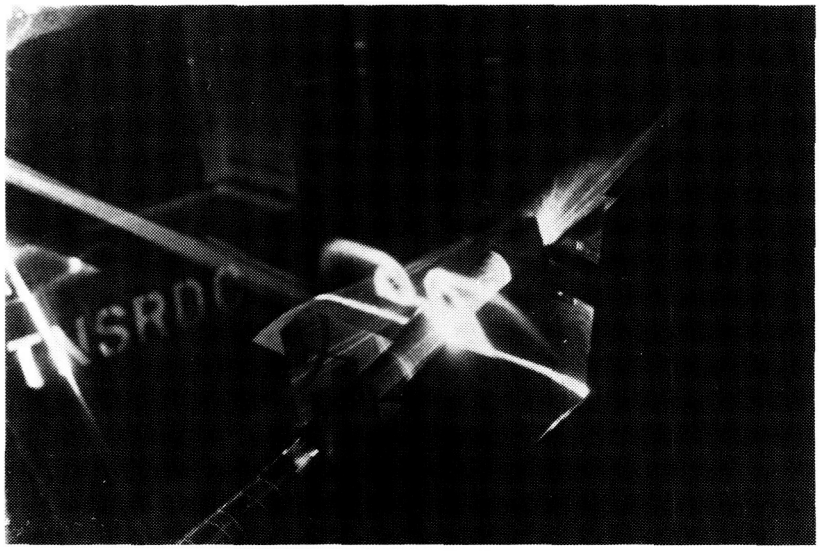


Figure 50. Laser vapor screen photograph as observed from a three-quarter right rear view. $M_\infty = 0.95$, $\alpha = 30^0$.



Figure 51. Laser vapor screen photograph as observed from a three-quarter left rear view. $M_\infty = 1.10$, $\alpha = 20^0$.

ORIGINAL PAGE
BLACK AND WHITE PHOTOGRAPH

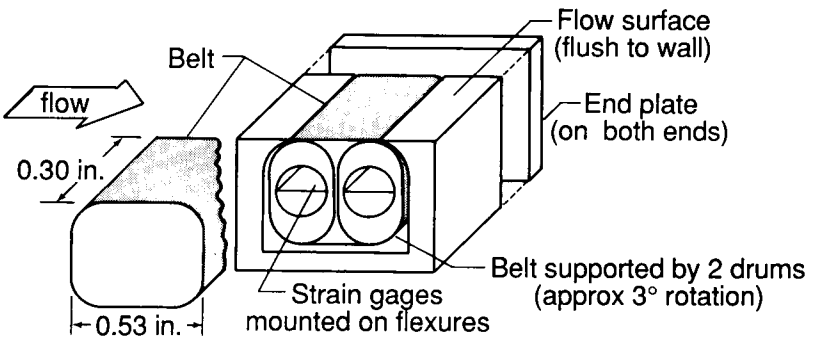


Figure 52. Sketch of the moving belt skin-friction gage showing its principal features.

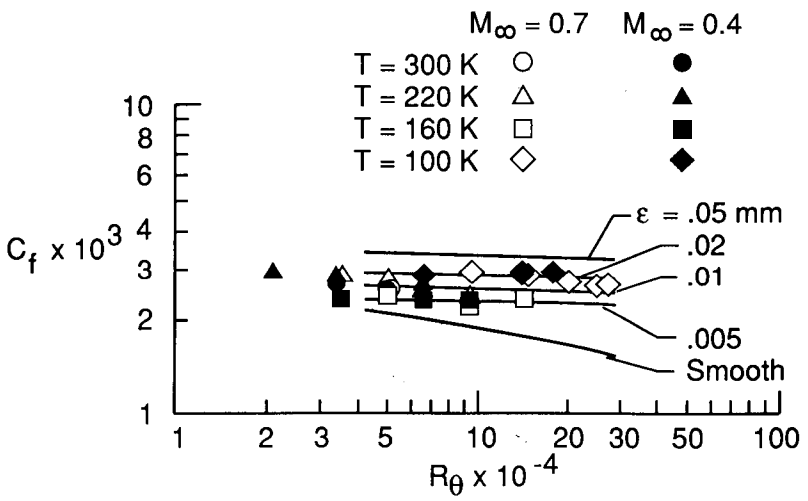


Figure 53. Plot of the variation of skin friction with Reynolds number based on momentum thickness.

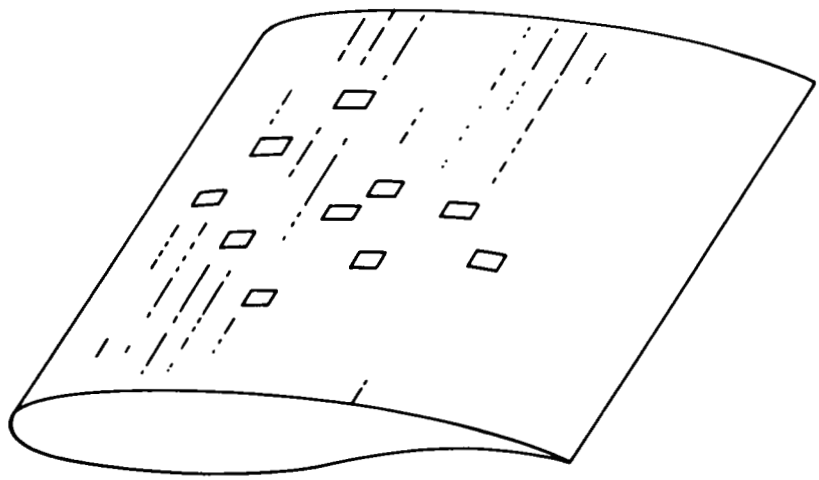


Figure 54. Sketch of an airfoil model with multiple skin-friction gages installed.